

# Numerical Wing/Store Interaction Analysis of a Parametric F16 Wing

Jens Cattarius

Dissertation submitted to the Faculty of the  
Virginia Polytechnic Institute and State University  
in partial fulfillment of the requirements for the degree of

Doctor of Philosophy  
in  
Engineering Mechanics

Dr. Daniel J. Inman, Co-Chair  
Dr. Dean T. Mook, Co-Chair  
Dr. Leonard Meirovitch  
Dr. Scott L. Hendricks  
Dr. Douglas K. Lindner

September 24, 1999  
Blacksburg, Virginia

Keywords: Aerodynamics, Aeroelasticity, Wing/Store Flutter,  
Vortex-Lattice Method, Decoupler Pylon  
Copyright 1999, Jens Cattarius

# Numerical Wing/Store Interaction Analysis of a Parametric F16 Wing

Jens Cattarius

(ABSTRACT)

A new numerical methodology to examine fluid-structure interaction of a wing/pylon/store system has been developed. The aeroelastic equation of motion of the complete system is solved iteratively in the time domain using a two-entity numerical code comprised of ABAQUS/Standard and the Unsteady-Vortex-Lattice Method. Both codes communicate through an iterative handshake procedure during which displacements and air loads are updated. For each increment in time the force/displacement equilibrium is found in this manner.

The wing, pylon, and store data considered in this analysis are based on an F16 configuration that was identified to induce flutter in flight at subsonic speeds. The wing structure is modeled as an elastic plate and pylon and store are rigid bodies. The store body is connected to the pylon through an elastic joint exercising pitch and yaw degrees of freedom. Vortex-Lattice theory featuring closed ring-vortices and continuous vortex shedding to form the wakes is employed to model the aerodynamics of wing, store, and pylon.

The methodology was validated against published data demonstrating excellent agreement with documented key phenomena of fluid-structure interaction. The model correctly predicts the effects of the pylon induced lateral flow disruption as well as wing-tip-vortex effects. It can identify the presence of aerodynamic interference between the store, pylon, and wing wakes and examine its significance with respect to the pressure and lift forces on the participating bodies. An elementary flutter study was undertaken to examine the dynamic characteristics of a stiff production pylon at near-critical airspeeds versus those of a soft-in-pitch pylon. The simulation reproduced the stabilizing effect of the stiffness reduction in the pitch motion. This idea is based on the concept of the decoupler pylon, introduced by Reed and Foughner in 1978 and flight tested in the early 1980's.

# Dedication

To my wife, Melissa.

# Acknowledgments

Upon graduating with a Master of Science from the *Teschnische Universität Darmstadt* in Germany, I came to Virginia Tech in December of 1993 to work on a three month research project under Dr. Daniel J. Inman. It was my first trip to the United States — back then I could not have possibly imagined the turn my life was about to take. Almost six years have gone by since then, during which I have experienced many of the profoundest moments of my life. Now, as this exciting chapter of my life is coming to closure and a new one is about to begin, I would like to take the opportunity to thank the people who took part in making my *stay* in the US such a humbling experience of success.

Foremost, I want to thank my wife, Melissa, who I met five years ago at Country Night at the Marriott in Blacksburg. The love we have for each other is the meaning of my life and without her all my accomplishments fade into obscurity. She endured many lonely nights and weekends at home while her husband struggled with lift coefficients and wake singularities. Thank you, Melissa, for the beautiful smiles I could always count on to make *today* a better day. Our marriage in June of this year has been the happiest day in my life — and I know, there are many more happy days to come.

I would like to express my deepest gratitude to Dr. Daniel J. Inman who took me under his wings and whose invigorating charisma prompted me to continue my academic education. His professionalism, genuineness, and trust together with a dazzling sense of humor are a true inspiration to all his students. I am most grateful for the five and one half years under his guidance, knowing that without his support I would not be where I am now. It is my sincere hope that we can continue working together beyond the boundaries of this appointment.

My thankfulness also goes to Dr. Leonard Meirovitch, Dr. Scott L. Hendricks, Dr. Romesh C. Batra, Dr. Dean T. Mook, and Dr. Douglas K. Lindner, my committee members, who have provided educational guidance and incentive through course work or through valuable advice regarding my research.

To this extent, I would like to express my deepest appreciation to Don Leo and Sergio Carneiro who I hold in highest regards, and who have been exceptionally helpful in catalyzing my thoughts and ideas. Don, having you as a friend has been inspirational and I will always cherish the hour-long discussions we indulged in over the ins and outs of life: we will somehow have to find a substitute for our weekly breakfast at Gillie's! Sergio, as my officemate you

bravely held out against invasions of flutter boundaries and wing-tip vortices — you have been a true friend and I will miss the many alluring conversations we had about research and life.

Many thanks to my current and former officemates at CIMSS who, as a group, have shared and continue to share help and support to make the individual ups and downs we all go through so much easier to bear. Especially the Mike’s-loving group of “Friday Engineers” made for a revitalizing conclusion of a hard week behind books and computer screens. Special thanks to Eric Austin who has been a mentor and good friend for the past five years. His professional experience and sound engineering knowledge have been an important resource in many aspects of my research. I would also like to express my gratefulness to Beth Howell, our Program Manager at CIMSS, who kept everything together when my brain was overwhelmed with countless deadlines.

I would also like to thank the group of former Buffalo MSL students who, when I first came to Virginia Tech, accepted me as one of their own and made it so easy for me to grab hold in an unfamiliar environment. I especially enjoyed our afternoon soccer games and the tubing trips to the New River! Heartfelt thanks to Don Leo and Ralph Rietz who have become dear friends of mine and with whom I spent many nights enchanting the three B’s of life. Without you, I probably would have never discovered the Country Night at the Marriott! Ralph, thank you for supplying *Brot und Wurst* from the local butcher in Buffalo — I will never forget the mouth-watering *Brotzeiten* it enabled me to enjoy thousands of miles away from home.

I want to send a warm thank-you across the ocean to the many friends that have kept in touch with me and that supported me throughout all these years. In particular, I would like to thank all of my family and friends who came to visit with us in Blacksburg. Being able to share this important part of my life with you has been a deeply gratifying experience. Special thanks to my former Handball team *TuS Wörrstadt* who flew me in for the season finale in 1994 and to help celebrate the league’s championship.

Last but not least I want to thank my parents who saw their son travel to America for three months and return six years later with a wife, who they love very much, a Ph.D., and a job. Your love and support always guided me in finding my little spot in the world. Thank you to all of my family abroad and in the US, your support and kind encouragement provided the essential foundation to thrive and succeed.

This work was supported by AFOSR grant number F49620-95-1-0362 managed by Maj. Brian Sanders. In additions, the final stages were supported by AFOSR grant number F49620-99-1-0294 managed by Maj. Brian Sanders and jointly supported by DARPA under the direction of Dr. E. Garcia for which the author is grateful.

# Contents

<b>1</b>	<b>Introduction</b>	<b>1</b>
1.1	History of Store-Flutter . . . . .	1
1.2	Objective of this Work . . . . .	5
1.3	Overview . . . . .	7
<b>2</b>	<b>Aerodynamics</b>	<b>10</b>
2.1	General Aerodynamics . . . . .	10
2.1.1	Fundamental Continuum Equations . . . . .	10
2.1.2	Stress in a Fluid . . . . .	11
2.1.3	Newtonian Fluid . . . . .	11
2.1.4	Navier-Stokes Equations . . . . .	13
2.1.5	Euler's Equations . . . . .	14
2.1.6	Potential Equations . . . . .	14
2.2	Unsteady-Vortex-Lattice Method (UVLM) . . . . .	16
2.2.1	Coordinate Systems . . . . .	18
2.2.2	The Model Discretization . . . . .	18
2.2.3	The Biot-Savart Law . . . . .	20
2.2.4	Working with Singularities . . . . .	22
2.2.5	Wake Development . . . . .	23
2.2.6	The Unsteady Bernoulli Equation . . . . .	24
<b>3</b>	<b>Numerical Model</b>	<b>30</b>

3.1	Structure . . . . .	30
3.1.1	ABAQUS/Standard . . . . .	30
3.1.2	The Structural Model . . . . .	31
3.2	The Aerodynamic Model . . . . .	35
<b>4</b>	<b>Aeroelasticity</b>	<b>39</b>
4.1	Equation of Motion . . . . .	39
4.2	Handshake . . . . .	40
4.3	Solution in Time . . . . .	42
<b>5</b>	<b>Results</b>	<b>47</b>
5.1	Static Analysis and Verification . . . . .	47
5.2	Clean Wing vs. Configured Wing . . . . .	50
5.3	Wake Analysis . . . . .	53
5.4	Dynamic Analysis . . . . .	56
<b>6</b>	<b>Summary, Contributions, and Future Work</b>	<b>62</b>
<b>A</b>	<b>Complementary Figures</b>	<b>73</b>

# List of Figures

2.1	Aerodynamic Lattice Model . . . . .	19
2.2	Example of Vortex-Lattice . . . . .	20
2.3	Finite Segment of a Straight Vortex Filament . . . . .	21
2.4	Velocity Field Induced by Vortex Filament . . . . .	21
2.5	“Viscous-Core” Vortex Velocity Field . . . . .	23
2.6	Velocities at Control Point . . . . .	26
2.7	Net-Value of the Velocity Potential Through Integration . . . . .	28
3.1	Flat Plate Wing Model Characteristics . . . . .	36
3.2	Bluff Store Model Characteristics . . . . .	37
4.1	Simulation Time Versus Iterations/Increments . . . . .	44
5.1	Wing Pressure Coefficient Distribution . . . . .	48
5.2	Verification of Wing Tip Vortex . . . . .	48
5.3	Store Pressure Coefficient Distribution . . . . .	49
5.4	Verification of Store Trailing Edge Wake . . . . .	50
5.5	Spanwise Static $C_L$ Distribution, Clean Wing and Configured Wing . . . . .	51
5.6	Effects of Wing Tip Vortex on Spanwise $C_L$ . . . . .	52
5.7	Lift Reduction due to Wing Configuration in Terms of $C_L$ . . . . .	52
5.8	Wake Plot for Dynamic Analysis . . . . .	53
5.9	Wake Plot for Dynamic Analysis . . . . .	54
5.10	Wake Plot Comparison for Dynamic Analysis . . . . .	55

5.11 Time History of Dynamic Lift on Wing . . . . .	55
5.12 Wing Tip Time Response for Production Pylon Model . . . . .	57
5.13 WPS Peak Deflection under Near Flutter Conditions . . . . .	57
5.14 Frequency Versus Velocity for Production Pylon Model . . . . .	58
5.15 Decoupler Pylon Model Versus Production Pylon Model . . . . .	59
5.16 Full Aerodynamic Treatment Versus Partial Treatment . . . . .	60
A.1 Coordinate Systems . . . . .	73
A.2 Wing/Pylon/Store Dimensions . . . . .	74
A.3 Clamped-Symmetric Mode Shapes of PP Configuration . . . . .	75
A.4 Clamped-Symmetric Mode Shapes of DP Configuration . . . . .	76
A.5 Handshake Flow Chart . . . . .	77

# List of Tables

3.1	Store Model Inertia Properties. . . . .	33
3.2	Symmetric Mode Frequencies. . . . .	33
3.3	Wing Model Material Properties. . . . .	34
3.4	Clamped-Symmetric Mode Frequencies. . . . .	34
4.1	Convergence Analysis with CW Model. . . . .	45

# Chapter 1

## Introduction

### 1.1 History of Store-Flutter

The problems resulting from wing/store interaction in aviation, in particular military aviation have been a prominent topic in the aerodynamic community for decades. Many different approaches to understanding and solving these problems have been undertaken by researchers. But the complexity of the interplay of aerodynamics and structure has yet kept researchers from developing truly reliable concepts that can eliminate the unwanted and oftentimes dangerous effects of self-induced oscillations of configured wings.

Flutter typically occurs upon coupling of the fundamental wing-bending frequency with either the wing-torsion or the store-pitch frequency. With increasing air speed, i.e., increasing dynamic pressure, wing-torsion, store-pitch, and wing-bending frequencies change, and eventually the latter can coincide with either or both wing-torsion or store-pitch frequencies. At this critical speed, where two natural frequencies attune, flutter is likely to occur.

Underwing mounted stores, such as engines, external fuel tanks, and missiles, have the common effect of lowering both the fundamental wing-bending and -torsion frequencies. The torsional frequency is lowered more significantly, thus reducing the separation between bending and torsion frequencies. As a result, with increasing airspeed the critical speed at which the two frequencies meet is reached sooner, and flutter can become a threat even within the normal flight envelope.

Throughout the years a variety of analytical control schemes have been investigated, aimed at suppressing wing flutter through active counter-mechanisms. They have been developed analytically and tested on wind-tunnel models and sometimes in flight on full-scale aircraft. The most common of these procedures act on “wing-owned” control surfaces, such as ailerons, flaperons, trailing-edge flaps, and/or leading-edge flaps.

In the 1970’s and throughout the early 1980’s, wing/store flutter was a very prominent

research topic, and many advances were made. Much of the research at the time was conducted in wind tunnels and validated in flight. Numerical analysis was more a means of initial design justification rather than a developers tool. In the mid 1980's focus began to shift from in-flight testing toward numerical analysis. Advances in computing power led to new numerical methods, many of which were used to develop improved control mechanisms. Wind tunnel tests were now the primary means of validation. Today the topic of wing/store-flutter control continues to be of interest, but mainly from an analytical standpoint. It seems that most published research deals with improving existing concepts in terms of reliability and robustness, rather than introducing new and innovative concepts. High-performance computers provide the grounds for advanced analysis and will eventually lead to reliable numerical methods for determining flutter boundaries and suppression systems.

The following is a short historical overview of some of the most significant developments in the field of wing/store flutter. Since some of the material is considered sensitive, if not classified, data were sometimes difficult or impossible to access by the author. Therefore, completeness of references can not be claimed.

In 1973 Triplett et al. [77] from *McDonnell Aircraft Company* first investigated analytically the possibility of adaptable wing/store flutter suppression using adjustable compensation in the feedback loop. Four different wing/store combinations were examined, each of which had its own designated compensator design. One accelerometer was placed at a wing-tip location, and the accelerometer signal was fed to the compensator, after integration, through a high-pass filter. A high-pass filter is required to decouple the pilot's commands from the control system. Typically wing/store flutter occurs at frequencies between 7–11 Hz so that the response of the flutter control system can be attenuated at low frequencies without compromising its performance. The control actuation was designed to continuously oppose wing deformation at the accelerometer location through aileron deflection. Results show that flutter can be stabilized with adequate stability margins despite the large number of model uncertainties.

In 1975 Hönlinger [38] under support from *Messerschmitt-Bölkow-Blohm* (MBB) installed forward vanes to external stores with the intention of using aerodynamic forces to suppress the onset of flutter. In 1977 their Flutter Suppression System (FSS) was successfully implemented and tested in flight on a Fiat F91/T3. The control scheme employed simple velocity feedback control, where the measured velocity of the store-pitch motion actuated the store vanes through a manually configured phase shift device. Feedback signals were produced by two accelerometers located in the forward and aft regions of the store. Results showed that an increase in damping was achieved through the aerodynamic counter-mechanism in the store-pitch motion.

This project was followed by a program that was launched in a cooperation of MBB and the *Bundesamt für Wehrtechnik und Beschaffung* in 1977 “to develop and flight test a system for store flutter suppression which could become a possible candidate for operational systems,” Sensburg et al. [70]. This time, existing control surfaces (ailerons) were to be

used to suppress flutter, and the control law was an optimal control design developed by MBB that received its input data from two accelerometers on the wing. In 1982, Sensburg et al. [71] of MBB together with *Air Force Wright Aeronautical Laboratories (Wright Labs)* published a paper on the results from flight test of an F-4F aircraft of the German Air Force. They demonstrated elastic mode suppression for low-frequency oscillations (5 Hz) under closed-loop tests. Higher frequencies (8 Hz) were unaffected by the FSS.

In 1979 Reed et al. [63] of *NASA Langley Research Center* introduced the so-called decoupler pylon which mounted stores elastically to the wing, in contrast to the standard rigid connection. The idea was to decouple the store from the wing by using an elastic pylon and, with that, restore the performance capabilities of the wing. Simulations and wind-tunnel tests (Reed et al. [62]) verified the potential of the method; it offered a practical alternative to previously pursued wing-based methods. After the initial success of the concept, Desmarais and Reed [18] in 1980 examined analytically the influence of pylon stiffness nonlinearities on the flutter characteristics of wing-mounted external stores because under rapidly changing transient loads the decoupler pylon can momentarily saturate when bottoming against a relatively stiff backup structure. The findings are summarized in terms of flutter suppression effectiveness and indicate that flutter speeds are raised by the decoupler pylon, even when its stiffness is inherently nonlinear. Limit-cycle behavior was not a subject of the study. Ground vibration tests of the decoupler pylon in 1986 (Cazier and Kehoe [11, 8]) were followed by flight tests with an F16 during which the original design was modified to host an alignment system (adjustable spring stiffness), resulting in a new semiactive decoupler pylon (Cazier and Kehoe [10]). It aimed at increasing the system's tolerance to changing air and maneuver loads by keeping the store in a nominally aligned static position. The flight tests demonstrated a 37% increase in flutter speed over conventional store attachments.

Around the same time as the introduction of the decoupler-ylon, Harvey et al. [32] of *Honeywell Incorporated*, together with *Wright Labs*, first investigated the possibility of truly adaptive wing/store flutter methods using a simplified analytical model of a YF-17 semispan wind-tunnel model. Their research featured adaptive algorithms of the Least Squares Discriminator, the Maximum Likelihood Estimator, and the Self-Tuning Regulator. Their adaptive technology was limited to “discrimination” and “adaptation to parameter uncertainty” and did not include the capability to identify a changing model. They concluded that adaptive control is feasible, but requires a significant amount of testing, preferably in the wind tunnel.

In 1980 and 1981 Noll et al. [55, 56] of *Wright Labs* investigated the performance of “international control laws” on the flutter suppression of the above-mentioned YF-17 semispan wind-tunnel model. Their investigation included five control laws: Northrop N3, Northrop N1, ONERA, B.Ae, and MBB. They concluded that all five control laws worked reasonably well, but were very susceptible to changes in Mach number, leading to instabilities.

One year later, Johnson et al. [40] from the *Massachusetts Institute of Technology* together with Harvey and Stein from *Honeywell Systems* published research using a self-tuning reg-

ulator for adaptive wing/store flutter suppression. The study examined the three different adaptive scenarios of constant plant parameters, slowly varying parameters, and abruptly changing parameters, i.e., store release. The STR concept offered a strong indication that control of wing/store flutter is feasible. Then in 1983, Johnson et al. [39] performed comprehensive tests of adaptive control algorithms for wing/store flutter suppression on a semispan wind-tunnel model. It included a store release scenario, and the method demonstrated that the adaptive algorithm recognized the unstable nature of the abrupt configuration change and implemented a stabilizing control law in a fraction of a second.

In 1989 one of the first publications to more closely examine pylon stiffness by means of analytical modeling as well as wind-tunnel tests was by Yang and Zhao [83] from *Northwestern Polytechnic University, Xian, China*. The work demonstrated, as had been observed by researchers before, that the pylon stiffness is a significant participant in wing/store flutter. According to their work, there are three types of flutter boundaries associated with wing/store flutter: type I can be attributed nearly to only the store itself, the wing motion induced could hardly be detected. Types II and III are very similar in nature (to each other), they both exhibit a sudden change in the flutter mode at one particular pylon stiffness. The flutter boundaries of type II depend strongly on the pylon stiffness. For this case, tuning the decoupler pylon to the optimal stiffness, can indeed increase flutter speeds significantly, even beyond that of the bare wing. Type III flutter boundaries, on the contrary, reveal a moderate and almost constant improvement in critical speeds over that of a wing with a rigidly attached store. Variations in pylon stiffness hardly have any effect with respect to flutter speed. In 1993 Yang et al. [84] examined effects of yaw and lateral pylon stiffness. Again they showed that there is a sudden change in flutter mode at a certain critical pylon stiffness. Unfortunately, they failed to identify what these flutter modes were.

Adaptive wing/store flutter suppression was again studied by Peloubet et al. [58]. The flutter model was an F16 full-span model that flew in the wind tunnel on a cable system. It employed flaperons at the wing's trailing edge that could be deflected symmetrically or differentially by the control mechanism. The FSS was designed to require no manual tuning or prior knowledge of the flutter modes, to be able to adapt to varying flight conditions, and to adapt to abrupt changes in the store configuration. System identification was achieved through a Canonical Variate Analysis, the order of the plant was selected through minimization of the Akaike Information Criteria, and the control law was computed by applying linear quadratic control law procedures. After successful testing for 3.5 weeks, the tests were terminated one day earlier than expected because of model failure due to control instabilities. Up to that point the AFSS had demonstrated great success in flutter suppression by increasing speeds up to 30% over the unaugmented (without flutter suppression) flutter boundaries for the three store configurations, including store release. However, the final failure of the system demonstrates how important it is to understand the mechanisms that cause store flutter.

In 1994 Gade and Flowers [24] from *Auburn University, AL* first investigated the possibilities of active flutter suppression by means of a "smart" pylon. Smart materials, such as piezoceramics and shape memory alloys, are easy to operate and require less space than equivalent

mechanical devices. The active concept is envisioned to improve flutter suppression of the semiactive decoupler pylon model and to provide an environment for controlled store release. Some examples of active material flutter suppression applications in aerospace engineering are: Main and Garcia [48], Ho and Chen [36], Heeg [33].

In the last three years, Gade and Inman from *Virginia Tech*, VA fortified the smart concept and developed a series of advanced control algorithms to suppress flutter based on the concept of piezoceramic stack actuators (Gade and Inman [26, 25, 28, 29, 30, 27]). The analytical strategies are based on simplified structural and aerodynamic models that cast out the complicated physics involved in the problem. Elaborate robustness studies involving uncertainty models were undertaken to compensate for the lack of model accuracy. Simulations provide encouraging results as to how flutter can be suppressed by application of the active “smart” decoupler pylon.

The following research is based on the knowledge gained from the original work by Gade and Inman with the decoupler pylon but shifts focus away from control and toward fundamental modelling issues.

## 1.2 Objective of this Work

The goal of this work is to develop a fully nonlinear aeroelastic analysis tool, that incorporates the most significant parameters identified by preceding wing/store research. These parameters are summarized and discussed below:

- Provide an aeroelastic model capable of examining the interplay of structural and aerodynamic nonlinearities.
- Provide the ability to investigate the importance of aerodynamic store effects under the prerogative of unsteady and nonlinear aeroelasticity.
- Provide the means to analyze wake-related phenomena such as wing-tip vortices and aerodynamic wake interference.

### Nonlinear Elements

The dominant nonlinearities are attributed to aerodynamics but, structural nonlinearities can play an important role as well. Effects such as backlash, freeplay, dry friction damping, actuator saturation, large displacements, etc., are some of the typical nonlinear aeroelastic elements that have been investigated by researchers (see Dowell and Ilgamov [19]). The effects of pylon pitch stiffness have been a reoccurring issue for wing/store flutter in the literature. Several researchers Yang et al. [84], Yang and Zhao [83], Zimmerman and Vogel [85], Sensburg et al. [71] have shown the pronounced effect pitch stiffness has on the flutter

speed. Nonlinearities in the pylon pitch stiffness have been considered by several authors, e.g., Cazier and Kehoe [10], Deferrari et al. [17], but their effects on limit-cycle oscillations (LCO) have only been reported fairly recently by Yang [82] of *Southwest Jiaotong University, China*. According to Mignolet et al. [49], such structural nonlinearities generally deserve much closer consideration in LCO research. In particular, nonlinear structural damping has been identified as a plausible mechanism involved in LCO behavior of the F16 (see Mignolet et al. [49], Chen and Liu [15]). However, structural nonlinearities have a controversial impact on flutter and LCO behavior of wing/store configurations.

The goal of the proposed research is to provide an analytical environment whereby such phenomena can be represented and investigated with great versatility. In particular for LCO research, this should enable researchers to shed some light on how structural nonlinearities dissipate a substantial amount of energy and thus provide a large stabilizing effect. For instance, Mignolet et al. [49] observed that wind-tunnel tests resulting in flutter often led to flight test resulting in LCOs.

## Store Aerodynamics

Another controversial subject is the contribution of store aerodynamics. Generally considered negligible, several researchers have shown that, under certain circumstances, it is necessary to include their influence (Özcan et al. [57], Chen and Liu [15], Turner [78], Roos [64], Vannunen et al. [81], Roos et al. [65], Bennekens et al. [3], van den Broek [79]). For instance, high-angle-of-attack applications lead to flow separation on the store surface that results in unsymmetric store loading. Investigations have been undertaken by Tang and Dowell [73], Triebstein et al. [75], Rusak et al. [66], and Almosnino and Rom [2], of whom the latter two included leading-edge-wake separation by means of the unsteady vortex-lattice method. When considering wake influences of wing/pylon/store configurations, the presence of a pylon/store combination has been shown to disrupt the trailing-edge wing wake, which in turn induces unsteady loads on the store body. The deformation of the wing wake, of course, also changes the loading on the wing itself (see Kayakayoglu [43]).

The aerodynamic model proposed for this study will include store and pylon aerodynamics so that their contribution to wing/store flutter can be examined when unsteadiness of forces and wake interferences are part of the model. Furthermore, the phenomenon of store flutter can only be explained when store aerodynamics are present. Such flutter exists and can lead to fatigue failure in the pylon as well as temporary inavailability of missiles in military applications. The sometimes violent nature of such oscillations can result in permanent damage to the complex guidance systems of missiles.

## Wake Contributions

Wake aerodynamics in wing/store flutter have generally not been considered. To the best of the author's knowledge, only Kayakayoglu [43] investigates the effects of an underwing store with respect to the wing-wake and the resulting effects on the pressure distribution on the bodies. Though the model does not include wake models for the pylon and store, it clearly identifies the contributions of wake dynamics for wing/store research. The author intends to continue down the same path but additionally include the contributions of cross-wake interference by modelling wing, pylon, and store wakes. In particular for wing/store interaction such interference is expected to be of great importance.

In summary, the author proposes a computational method that can enhance analytical modelling of wing/store interaction by due consideration of the phenomena mentioned above. To assess the capabilities of the "smart" pylon reliably, it is necessary modeling the physics of the problem accurately, particularly the interaction of fluid and structure. Currently available production codes encompass only a selection of these parameters and thus do not allow modeling of the aeroelastic nature of wing/store flutter in such a complete fashion: see Mignolet et al. [49].

## 1.3 Overview

The numerical model is constructed of two fundamental building blocks: the aerodynamic model and the structural model. Each model was chosen to best meet the demands imposed by the physics of the wing/store flutter problem. The choice for the structural model fell on ABAQUS/Standard, a comprehensive nonlinear finite element (FEM) package (Hib [34]). ABAQUS is well established as a powerful nonlinear finite element environment that offers versatility in structural modelling and a large variety of nonlinear analytical tools ranging from nonlinear geometric analysis to nonlinear elasticity.

The decision on the governing dynamic fluid equation was based on the flow field characteristics and flight conditions. For the case under investigation, it seemed favorable to include wake dynamics and, for future investigations, to allow for leading-edge separation at high-angle-of-incidence situations. From published research it is known that flutter and LCOs for configured fighter aircraft, such as the F16, start to occur at subsonic speeds. It is always advisable to choose the least complicated, adequate model that will describe the flow about the configuration being considered. The typical levels of flow approximation are;

1. Navier-Stokes
2. Euler
3. full potential (compressible)

#### 4. potential (incompressible)

Moving from the potential equation to the next higher level is accompanied by a substantial increase in analytical complexity and computational cost. Euler and Navier-Stokes codes are commonly referred to as computational fluid dynamics (CFD) and require modelling of the entire flow field. Such codes have only been in commercial use since the early 1980's Hicks et al. [35] and lack transparency and simplicity of application compared to potential-flow approximations. The grid generation for complex geometries itself, e.g., wing/store combinations, has become an engineering discipline, e.g., Chimera (see Holst [37]), that can stand on its own. Madson and Ericksons [47] state that "each new geometry demands a substantial amount of calendar time in the generation of the flow field grid, and there is the need to 'tweak' various parameters within the codes themselves in order to adjust them for each new geometry and flow condition." Potential-flow codes are more robust and receive a high level of confidence in the aerodynamic community due to the many decades of service. Their limitations are well understood and, depending on the flow environment, have no substantial impact on the accuracy of the solution when the codes are properly applied. When rotational and/or separated flow are of considerable importance to the flow field, CFD codes describe the aerodynamic characteristics usually more accurately. This can be the case for highly swept wings or high-angle-of-attack applications. Also for transonic applications where sub- and supersonic phenomena coexists, potential flow solvers are not a good choice. (An exception to this rule is TranAir, a full-potential solver for transonic flow about completely arbitrary geometries.)

After due consideration of the operational expertise required of the user as well as computational cost efficiency, it was concluded that a subsonic panel method in the form of the unsteady vortex-lattice-method (UVLM) would provide the best compromise between efficiency and accuracy. The aerodynamic part of an aeroelastic model designed by Preidikman and Mook [60] to investigate flutter on commercial aircraft served as a basis for the UVLM model employed here. Because of the different nature of the aeroelastic model at hand, substantial alterations and modifications were necessary to adapt Preidikman's model to the multibody wing/pylon/store system. The resulting model is unsteady, nonlinear, and provides the full wake as part of the solution. Leading-edge separation is not included here, but publications on how to extend the employed aerodynamic code are readily available (Mook and Nayfeh [52, 51], Almosnino [1], Nayfeh et al. [54]).

The effort reported here can be summarized by the following contributions to understanding the fluid-structure interaction of a wing/store system:

- Development of a new methodology for examining fluid-structure interaction for wing/store configurations.
- Modification and extension of a UVLM based aerodynamic code to include pylon and store aerodynamics.

- Development and implementation of a handshake mechanism to govern convolution of two independent software entities: structure and aerodynamics
- Development of the ability to consider both structural and aerodynamic nonlinearities in one model.
- Development of the ability to capture the history of the flow in the trailing-edge wake.
- Development of the ability to analyze wake-related phenomena such as wing-tip vortices and aerodynamic interference.

Furthermore, the developed code is benchmarked against several results in fluid-structure interaction.

# Chapter 2

# Aerodynamics

## 2.1 General Aerodynamics

### 2.1.1 Fundamental Continuum Equations

The fundamental equations in continuum mechanics are the balance equations. This text is concerned with fluid motions around an airplane which are best represented in the spatial or Eulerian description from a vehicle-fixed reference frame. Common tensor notation is used for the following derivations. Hence, the first balance equation is the continuity equation, which expresses the principle of conservation of mass

$$\frac{D\rho}{Dt} + \rho v_{j,j} = 0 . \tag{2.1}$$

The mass-balance is derived from the fact that the mass of the continuum in any chosen control volume does not change with time. The material density is  $\rho$ ,  $v_i$  are the velocity components of the continuum, and  $\frac{D}{Dt}$  is the material derivative, i.e.,

$$\frac{D\alpha}{Dt} = \frac{\partial\alpha}{\partial t} + v_j \alpha_{,j} .$$

The second fundamental balance equation is the principle of conservation of linear momentum which yields the equation of motion for fluid flow

$$T_{ij,j} + \rho f_i = \rho \left( \frac{\partial v_i}{\partial t} + v_j v_{i,j} \right) . \tag{2.2}$$

$T_{ij}$  is the stress tensor defined in Section 2.1.2 and  $f_i$  are the body forces of the considered continuum, Lai et al. [46]. The third and final balance equation expresses the principle of conservation of energy, which for a Newtonian fluid, see Section 2.1.3, is of the form

$$\rho \frac{Du}{Dt} = T_{ij} v_{i,j} - \frac{\partial q_i}{\partial x_i} + q_s , \tag{2.3}$$

where  $u$  is the internal energy per unit mass,  $q_i$  are the components of the heat flux vector, and  $q_s$  is the heat supply due to external sources. The above three equations are fundamental to fluid flow and will be used in the following sections to derive the most common levels of fluid flow approximations used in aeroelasticity.

### 2.1.2 Stress in a Fluid

The difference between stress in a fluid and stress in a solid is that in a fluid the state of shear stress does not depend on the deformation itself, but rather on the rate of deformation. Thus, it is common practice to separate the stress tensor into two parts

$$T_{ij} = -p\delta_{ij} + T'_{ij}. \quad (2.4)$$

The viscous stress tensor  $T'_{ij}$  depends explicitly on the rate of deformation represented by the strain rate tensor

$$D_{ij} = \frac{1}{2}(v_{i,j} + v_{j,i}),$$

which in turn depends on the spatial partial derivatives of the velocity components  $v_i$  of the continuum. The pressure  $p$ , a scalar quantity, is part of the compressive normal stress on a plane and does not explicitly depend on  $D_{ij}$ . For compressible fluids,  $p$  is a function of the density  $\rho$  and the absolute thermodynamic temperature  $\theta$ , i.e., thermodynamic effects enter the system of equations. If compressibility can be neglected,  $p$  is merely the mean compressive normal stress, as discussed in Section 2.1.3.

### 2.1.3 Newtonian Fluid

A Newtonian fluid is defined by assuming a linear dependence of the viscous stress tensor  $T'_{ij}$  on the instantaneous value of the strain rate tensor  $D_{ij}$ . Hence, a Newtonian fluid is also called a linear viscous fluid. The viscous stress tensor takes the form,

$$T'_{ij} = \lambda D_{kk}\delta_{ij} + 2\mu D_{ij},$$

where  $\lambda$  and  $\mu$  are material constants associated with the viscosity of the fluid. Finally, the stress tensor for a linear viscous fluid can be assembled

$$T_{ij} = -p\delta_{ij} + \lambda D_{kk}\delta_{ij} + 2\mu D_{ij}. \quad (2.5)$$

This particular model of a fluid has been found to describe adequately the mechanical behavior of many real fluids under a wide variety of situations. The viscosity of Newtonian fluids is a true thermodynamic property and varies with density and temperature. Viscous flow properties in aeroelasticity are encountered near the surfaces of immersed bodies, where inside a thin layer (boundary layer) velocity gradients are large. This situation is due to the shear and no-slip condition associated with viscous flow.

### Incompressible Newtonian Fluid

Incompressibility implies that the density of a fluid does not change with time, i.e.,

$$\frac{D\rho}{Dt} = 0.$$

Substituting this into the continuity equation, (2.1), the following alternative statement of the incompressibility equation is found:

$$v_{j,j} = \operatorname{div} \mathbf{v} = 0, \quad (2.6)$$

which is equivalent to  $D_{kk} = 0$ , and the constitutive equation becomes

$$T_{ij} = -p\delta_{ij} + 2\mu D_{ij}. \quad (2.7)$$

Equation (2.7) allows derivation of an expression for the pressure  $p$ . It follows from  $T_{jj} = -3p + 2\mu D_{jj}$  that, for incompressible flow, the pressure is the mean normal compressive stress, i.e.,

$$p = -\frac{T_{jj}}{3}.$$

This holds for viscous as well as inviscid flow.

Incompressible flow covers the low range of flow speeds up to Mach numbers of approximately  $\text{Ma} = 0.5$ . In this region the fluid properties are continuous and density variations in most cases are negligible.

### Compressible Newtonian Fluid

When the flow is compressible, variations of the density of the fluid are no longer negligible. This requires thermodynamic effects to be considered in order to define pressure, in the most general case, as a function of density and temperature,  $p = p(\rho, \theta)$ . The thermodynamic phenomena are derivable from the state equation for ideal gases,

$$p = \rho R \theta,$$

in combination with the assumption of constant specific heat and that all processes are reversible. In the equation above,  $\rho$  is the density,  $R = c_p - c_v$  is the gas constant as a function of the specific heat constants, and  $\theta$  is the temperature. In most aerodynamic theory of interest to aeroelasticians, the thermodynamic properties of the gas enter only through the specific heat ratio  $\gamma = c_p/c_v$ , Bisplinghoff et al. [5].

In the absence of strong shocks or intense heating, the state equation simplifies to  $p \sim \rho^\gamma$ . This is the so-called isentropic flow assumption for which thermodynamic processes are reversible and adiabatic (nonheat conducting) and the pressure-density relation is explicit

and barotropic throughout the entire flow field. Isentropic flow is a valid assumption when the fluid originates in a reservoir under uniform stagnation conditions or when straight, parallel streamlines with constant ambient properties characterize the fluid motion upstream. Compressibility in aeroelasticity is usually required once the flow leaves the incompressible flow region,  $Ma > 0.5$  (Bisplinghoff et al. [5]), where  $Ma$  is the Mach number.

### 2.1.4 Navier-Stokes Equations

The well-known Navier-Stokes equation results when the stress tensor in Equation (2.2) is replaced by its constitutive definition for linear viscous flow, Equation (2.5). The body forces have been omitted, as is customary in heavier-than-air bodies in aeroelasticity.

$$-p_{,i} + (\lambda + \mu)v_{j,ji} + \mu v_{i,jj} = \rho \left( \frac{\partial v_i}{\partial t} + v_j v_{i,j} \right). \quad (2.8)$$

The equation is a nonlinear partial differential equation and is accompanied by the continuity equation, Equation (2.1), the energy equation, Equation (2.3), and the thermodynamic state equations,  $p = p(\rho, \theta)$  and  $u = u(\rho, \theta)$  to fully capture the mechanics of fluid flow. Closed-form solutions for the above set of equations exist only for a very limited number of examples. Aeroelasticians often resort to CFD to approximate fluid behavior numerically. The solution must be obtained everywhere in the flow field, which generally requires discretization in three dimensions. Physically the Navier-Stokes formulation captures much of the flow phenomena, some of which are of major interest to aeroelasticians, such as separated flow (leading-edge vortical flow), vortex flow (turbulence, wake shedding), shock waves, and boundary-layer effects. However, even for simple configurations such as airfoils, discretization to account for boundary-layer effects at high Reynolds Numbers requires the use of a very fine mesh in the direction normal to the surface to capture the extreme velocity gradients. For more complex configurations the process of grid generation becomes difficult at best, not to mention the process of actually solving for the velocity and pressure fields. The Navier-Stokes formulation can be classified as an expert-user code which normally requires a supercomputer to run successfully, Tinoco [74].

### Viscous Boundary Condition: No-Slip

As a result of viscosity, the flow past a body must assume the velocity of the body wherever they meet,

$$\mathbf{v}_{Fluid} = \mathbf{v}_{Body}. \quad (2.9)$$

This results in a thin layer with high velocity gradients in which the flow field adjusts from body velocity to freestream velocity — the boundary layer. When boundary-layer effects are responsible for separated flow along smooth surfaces due to high angles of attack, it can have a drastic influence on the global pattern of the flow. The boundary layer can also cause large changes in a lifting flow by changing the circulation.

### 2.1.5 Euler's Equations

Viscous effects are relatively unimportant outside the boundary layer under the assumption that the flow is *attached*. Thus in this situation it is of advantage to neglect these effects altogether and assume inviscid fluid properties. The fluid stress tensor takes the form

$$T_{ij} = -p\delta_{ij},$$

and inserting this into Equation (2.2), one obtains Euler's equation:

$$-p_{,i} = \rho\left(\frac{\partial v_i}{\partial t} + v_j v_{i,j}\right). \quad (2.10)$$

Equation (2.10) is still nonlinear, and, just as for Equation (2.8), the solution requires numerical methods utilizing three-dimensional grids for three-dimensional bodies. The Euler formulation represents the highest inviscid approximation to the Navier-Stokes Equation. As a result, nonisentropic shocks and rotational flow regions can be part of the solution. Of course the precise structure of the computed shocks and the rotational flow regions is inaccurate because the viscous terms are absent. Inviscid flow properties also affect the ability to approximate skin friction drag which depends on viscous effects. (Form drag, drag due to lift, and induced drag are not affected by omitting viscosity.)

#### Inviscid Boundary Condition: No-Penetration

The aerodynamic method models the flow outside the boundary layers (the so-called outer flow); consequently, only the no-penetration boundary condition is imposed. Now only the normal components of the velocities of the body and the flow need to be matched, yielding

$$\mathbf{v}_{Fluid} \cdot \mathbf{n} = \mathbf{v}_{Body} \cdot \mathbf{n}, \quad (2.11)$$

where  $\mathbf{n}$  is the unit normal to the body's surface.

### 2.1.6 Potential Equations

The next lower level of approximation to the Navier-Stokes equation is reached by assuming that the outer flow is inviscid. As a result all fluid particles have zero angular momentum for all time, and this is expressed mathematically by the disappearance of the curl of the velocity vector,

$$\nabla \times \mathbf{v} = \mathbf{0}.$$

In light of the fact that the curl of the gradient of any scalar function is by definition always zero, the three velocity components  $v_i$  can be bundled into one scalar function. By setting

$v_i = \phi_{,i}$  (or  $\mathbf{v} = \nabla\phi$ ) where  $\phi$  is the velocity potential, the condition of irrotational flow is automatically satisfied, i.e.,

$$\nabla \times \mathbf{v} = \nabla \times \nabla\phi = \mathbf{0}$$

for any  $\phi$ . Inserting the velocity potential into Euler's equation yields

$$-p_{,i} = \rho \left( \frac{\partial \phi_{,i}}{\partial t} + \phi_{,j} \phi_{,ij} \right),$$

which can be rewritten as

$$\frac{\partial}{\partial x_i} \left[ \int \frac{dp}{\rho} + \frac{1}{2} \left( \frac{\partial \phi}{\partial x_j} \frac{\partial \phi}{\partial x_j} \right) + \frac{\partial \phi}{\partial t} \right] = 0, \quad (2.12)$$

where  $\frac{1}{\rho} \nabla p = \nabla \left( \int \frac{dp}{\rho} \right)$  has been introduced, see Currie [16]. Integration of the irrotational Euler equation, Equation (2.12), yields Kelvin's equation

$$\frac{\partial \phi}{\partial t} + \int \frac{dp}{\rho} + \frac{1}{2} \left( \frac{\partial \phi}{\partial x_j} \frac{\partial \phi}{\partial x_j} \right) = F(t), \quad (2.13)$$

which resembles the integrated form of the equation of motion and provides the solution for the pressure field, once the velocity field is established. Further mathematical manipulations of Equation (2.13) together with the continuity equation, Equation (2.1), will lead to the full potential equation, see, e.g., Bisplinghoff et al. [5]. It is the exact nonlinear, unsteady-flow equation to be satisfied by the velocity potential

$$\nabla^2 \phi - \frac{1}{c^2} \left[ \frac{\partial^2 \phi}{\partial t^2} + \frac{\partial q^2}{\partial t} + \nabla \phi \cdot \nabla \left( \frac{q^2}{2} \right) \right] = 0, \quad (2.14)$$

where  $c^2 = dp/d\rho$  is the local speed of sound and  $q^2 = \mathbf{v} \cdot \mathbf{v}$ . Next, the equation is linearized by introducing "small velocity disturbance" approximations and steadiness of the formulation is assumed. Thus, the linearized potential equation for subsonic and supersonic flow, where  $\text{Ma}$  is the local Mach number, is obtained

$$\nabla^2 \phi - \text{Ma}^2 \phi_{,11} = 0. \quad (2.15)$$

The flow governed by the linearized potential equation, Equation (2.15), is restricted to steady, irrotational, inviscid, isentropic, and nontransonic flow within the linear range of its dependent variables. These conditions restrict the flow physics to steady-state attached flow but because compressibility has not been ruled out completely, the presence of weak shocks permitting isentropic jumps can be approximated satisfactorily.

To reach yet an even further simplified level of approximation to Equation (2.8), the fluid, on top of all previous simplifications, is assumed incompressible a consequence of which is that  $c$  in Equation (2.14) is infinite. Then Equation (2.14) reduces to

$$\nabla^2 \phi = 0. \quad (2.16)$$

Beside the obvious mathematical simplifications achieved by potential formulations, they owe their success in aerodynamics to the fact that they accurately describe the velocity field for many important applications. In conjunction with the proper boundary conditions, calculating the velocities from the potential form of the continuity equation is a much easier task than solving a set of partial differential equations, as required for higher order formulations. As mentioned above, with the velocity field known, Kelvin's equations provides the solution for the pressure field in the form of a simple algebraic relationship. In fact, with the incompressibility condition valid, Kelvin's equation, Equation (2.13), simplifies to the unsteady Bernoulli equation:

$$\frac{\partial \phi}{\partial t} + \frac{p}{\rho} + \frac{1}{2}v_j v_j = \text{const.} \quad (2.17)$$

By means of the divergence theorem, all characteristics of the three-dimensional flow field can be deduced from surface integrals over the immersed body. This opened the way to the development of various panel methods, which allow a “quick and easy” assessment of an aircraft's aerodynamic characteristics. The surface of an aircraft is normally discretized into flat, panels each of which contain constant-strength singularities (linear panel methods) which guide the freestream around the geometry of the body. Doublet singularities are commonly employed to describe lifting surfaces (zero thickness) and sources are used to generate nonlifting, three-dimensional surfaces. Use of linear panel methods dates back to the late 1960's. Over the past 30 years, panel methods have matured and today are very well understood and receive a high level of confidence in the aerodynamic community. Today, higher order panel methods that aim at satisfying “exact to surface” boundary conditions are available. In addition complementary tools have been developed to overcome some of the shortcomings of potential equation based algorithms, e.g., boundary-layer correction. Among the most commonly used commercial panel codes are PanAir, Cenko [12], Cenko and Tinoco [13], Cenko et al. [14] and HISSS, Fornasier [23].

A cousin to the classical panel methods is TranAir, see Samant et al. [68]. It employs the surface paneling technique together with a three-dimensional flow field grid needed for higher level approximations to Equation (2.8). It was primarily designed to analyze complex configurations in the transonic flight range, where subsonic and supersonic flow phenomena coexist.

## 2.2 Unsteady-Vortex-Lattice Method (UVLM)

The vortex-lattice method is based on the fundamental physical observation that the flow past immersed bodies generates vorticity along surfaces in contact with the flow. For attached flow this effect is confined inside a thin boundary layer. The vorticity leaves the boundary layer to enter the freestream only where there is separation, which is assumed to occur at trailing edges or other sharp edges, and forms the trailing vortex sheet or wake. The

boundary layer itself need not be modeled explicitly but its implicit effects on the global flow mechanics are fully accounted for. Meaning that the global flow can actually be regarded as being inviscid, confining vorticity to the boundary layers and the wake. The only shortcoming resulting from this assumption is that in the case of separated flow, the location of the separation is not provided as part of the solution. The locations must be specified apriori in the sense of an extended boundary condition, providing a means of analyzing separated flow. References Preidikman [59], Mook and Nuhait [53], Konstadinopoulos et al. [44, 45] explain the general formulation of the UVLM employed in this research. The following sections provide derivations of the fundamental principles of the UVLM and outline how the method is related to the specific model employed here.

The vortex-lattice method takes advantage of the direct kinematic relationship between the global velocity field and the vorticity produced by the shear forces on the body boundaries due to that same velocity field (see Biot-Savart law in Section 2.2.3). However, fundamental to this relationship is the mathematical concept of incompressibility, governed by Equation (2.6). Recalling the definition of vorticity,

$$\boldsymbol{\Omega} = \nabla \times \boldsymbol{v}, \quad (2.18)$$

and defining  $\boldsymbol{v} = \nabla \times \boldsymbol{A}$ , where  $\boldsymbol{A}$  can be any divergenceless ( $\nabla \cdot \boldsymbol{A} = 0$ ) vector field, the vorticity vector can be expressed as

$$\boldsymbol{\Omega} = -\nabla^2 \boldsymbol{A}. \quad (2.19)$$

This definition of  $\boldsymbol{v}$  takes advantage of the mathematical fact that the divergence of the curl of any vector field is always zero. Based on the incompressibility assumption, the equation

$$\nabla \cdot \boldsymbol{v} = \nabla \cdot \nabla \times \boldsymbol{A} = 0$$

holds for any  $\boldsymbol{A}$ . (In order to arrive at Equation (2.19),  $\boldsymbol{A}$  must be divergenceless, such that  $\nabla \times \nabla \boldsymbol{A} = -\nabla^2 \boldsymbol{A}$  is true.)

Equation (2.19) can be integrated to solve for  $\boldsymbol{A}$  in terms of the vorticity. Leaving the vorticity confined inside the boundary layer as the true unknown in this formulation. The vorticity is obtained by imposing no-penetration conditions along body boundaries, i.e., utilizing the fact that the flow field must not enter (penetrate) the immersed body. As with the potential equations, the solution of the velocity field does not require the equation of motion. Much like the paneling of potential methods the boundary layers on the body surfaces are discretized into a lattice of finite constant vortex segments. The vortex-lattice method thereby shares the advantages of the potential solutions while avoiding some of their shortcomings. The main restriction lies in the incompressibility assumption, which makes it impossible to capture shock waves and the drag associated with them. The flow speed must be kept within the subsonic range. On the other hand, unlike potential flow, steadiness, attached flow, and small perturbation assumptions are not required. Furthermore the vortex-lattice method also yields the wake as part of the solution and is capable of accurately approximating flow interference due to the shedding of vorticity.

### 2.2.1 Coordinate Systems

The equation of motion of the complete system is expressed in terms of a body-fixed (BF) coordinate system that is attached to the airplane along the plane of symmetry, as depicted in Figure A.1 of the Appendix. The x-axis extends from the trailing edge forward, the y-axis lies along the wing span, and the z-axis points down, perpendicular to both y- and x-axis. A Newtonian reference (NR) frame is fixed in the far field to the uniform freestream. Because Bernoulli's equation, however, is formulated in the NR frame it is necessary to perform a transformation between the two coordinate systems. The position vectors to a particular point on the body obey the following relationship:

$$\mathbf{r} = \mathbf{r}^{BF} + \mathbf{r}^*,$$

and taking the total derivative yields,

$$\mathbf{v} = \mathbf{v}^{BF} + (\boldsymbol{\omega}^* \times \mathbf{r}^*) + \mathbf{v}^*. \quad (2.20)$$

Quantity  $\mathbf{v}^{BF}$  is the velocity of the body-fixed frame with respect to the NR frame,  $\boldsymbol{\omega}^*$  is the angular velocity of the moving frame, and  $\mathbf{v}^*$  is the velocity of the material point in terms of the B-F frame. The current model does not support angular motion of the airplane, eliminating contributions by  $\boldsymbol{\omega}^*$  from Equation (2.20). Noting that the component  $\mathbf{v}^{BF}$  is the forward speed of the airplane or simply the negative of the freestream velocity  $V_\infty$  as introduced in preceding chapters, Equation (2.20) reduces to

$$\mathbf{v} = -\mathbf{V}_\infty + \mathbf{v}^*.$$

The above transformation is needed to convert control-point velocities  $\mathbf{v}_{CP}^*$  which are obtained in the BF frame, i.e.,  $\mathbf{v}_{CP} = -\mathbf{V}_\infty + \mathbf{v}_{CP}^*$ . Total derivatives with respect to time are required for the unsteady portion of Bernoulli's equation and are more fit to be discussed there. Please refer to Section 2.2.6.

### 2.2.2 The Model Discretization

The UVLM discretizes the model surfaces into discrete lattices, where the lattice segments are finite-length, straight vortex filaments of constant circulation  $\gamma$ . In Figure 2.1 the lattice for the wing/pylon/store model under investigation is represented. Each set of four (three for the leading edge of the store) connecting segments forms a surface panel or vortex "ring" of constant circulation  $G_i$ , where  $i$  is the index of the active panel. The circulation vector  $\mathbf{G}$  is one dimensional and of length  $N = \text{"number of panels"}$ . It constitutes the fundamental quantity of the UVLM from which every other quantity is derived through purely algebraic relationships. The strength of  $\mathbf{G}$  can be determined uniquely by enforcing the no-penetration condition, Equation (2.11), at one point in every panel. This point is called the control point and is the centroid of the panels.  $\mathbf{v}_{Body}$  therefore is a vector of resultant velocities at the

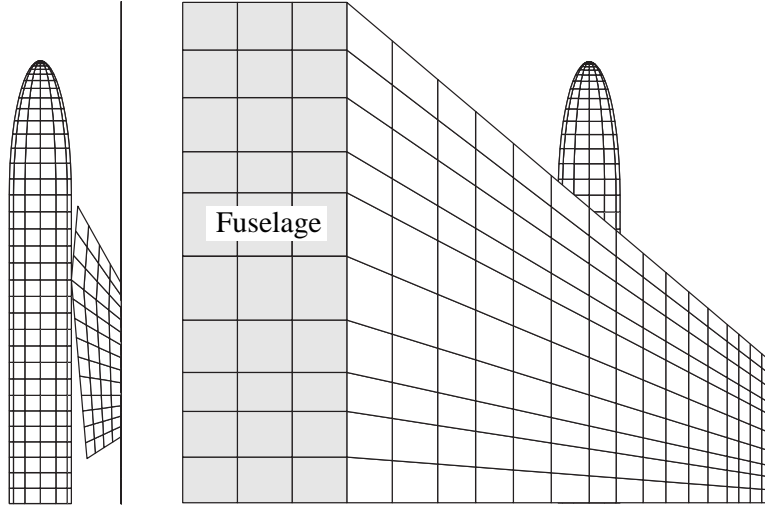


Figure 2.1: Aerodynamic Lattice Model

panel control points and will be denoted by  $\mathbf{v}_{CP}$ . As discussed in the previous section, this is the NR frame value of the control-point velocities and is composed of  $(-\mathbf{V}_\infty + \mathbf{v}_{CP}^*)$ . The induced velocities that stem from all vortex rings that represent the body, or bound vortex  $\mathbf{v}_{BL}$ , plus all induced velocities that stem from the vortex rings that form the wake, or free vortex,  $\mathbf{v}_{WK}$  represent the fluid particle velocities  $\mathbf{v}$ . The no-penetration condition can be rewritten in the form

$$\left\{ \underbrace{(\mathbf{v}_{BL} + \mathbf{v}_{WK})}_{\mathbf{v}_{mean}} \cdot \mathbf{n} \right\}_i = \left\{ (-\mathbf{V}_\infty + \mathbf{v}_{CP}^*) \cdot \mathbf{n} \right\}_i. \quad (2.21)$$

In this form, it states that the normal components of the mean flow velocities,  $\mathbf{v}_{mean}$ , see Section 2.2.6, must equal the normal component of the body velocities at every control point. Using the fact that the normal velocities induced by the bound vortex  $\mathbf{v}_{BL}$  can be rewritten in terms of a matrix of influence coefficients  $A_{ij}$  and panel circulations  $G_i$ ,

$$\{\mathbf{v}_{BL} \cdot \mathbf{n}\}_i = \sum_{j=1}^N A_{ij} G_j \quad \text{with } i = 1 \dots N. \quad (2.22)$$

Equation (2.21) can now be expressed in terms of  $\mathbf{G}$ ,

$$\sum_{j=1}^N A_{ij} G_j = \{(-\mathbf{V}_\infty + \mathbf{v}_{CP}^* - \mathbf{v}_{WK}) \cdot \mathbf{n}\}_i. \quad (2.23)$$

Matrix  $A_{ij}$ , calculated by use of the Biot-Savart law of Section 2.2.3, captures the velocity at the control point of panel  $i$  induced by the unit-circulation vortex ring of panel  $j$ . The

influence matrix depends on the shape of the mesh and the control-point velocities, i.e., the positions, dimensions, and velocities of the lattice segments. Generally the matrix is not symmetric, particularly when the bodies are subject to deformation. To solve Equation (2.23) for  $G_i$ , the influence matrix must be inverted; the UVLM employs a standard LU-decomposition to accomplish this task.

After determining the circulation associated with each panel, i.e.,  $G_i$ , it is a simple matter of adding or subtracting adjoining “panel strengths” to obtain the circulation of the finite vortex lattice filaments  $\gamma_k$  that the panels share. In Figure 2.2 the finite vortex filaments are depicted by white arrows and the panel vortex “rings” by black arrows that circumscribe the panel boundaries in the clockwise direction. For the case displayed here,  $\gamma_i$  would simply equal  $(G_j - G_i)$ . The direction of positive vorticity of the lattice, defined here from left to right and from bottom to top, is arbitrary but must be consistent throughout the model.

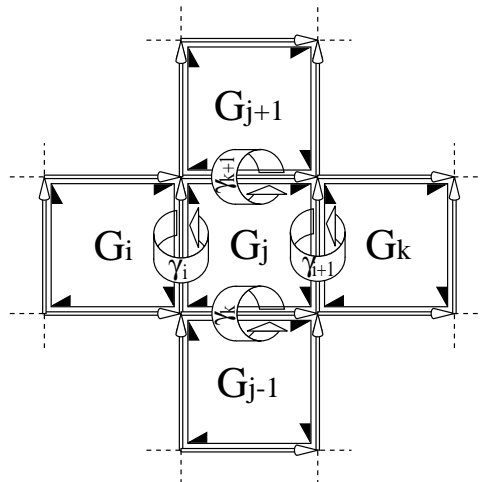


Figure 2.2: Example of Vortex-Lattice

This defines the vortex lattice that is now used to calculate the induced velocities at the control points of each panel via the Biot-Savart law.

### 2.2.3 The Biot-Savart Law

One can use the Biot-Savart law to obtain the velocity at any point P in the flow associated with a vortex filament. Due to the spatial conservation of vorticity, a vortex filament cannot begin or end abruptly in a fluid. “It should either form a closed ring or end at infinity or at a solid or free surface,” Karamcheti [42]. Therefore, the UVLM uses closed quadrilateral or triangular vortex “rings” to model the boundary layers of the bodies and the free wakes. Each such “ring” can be pictured to be formed out of four or three discrete vortex filaments

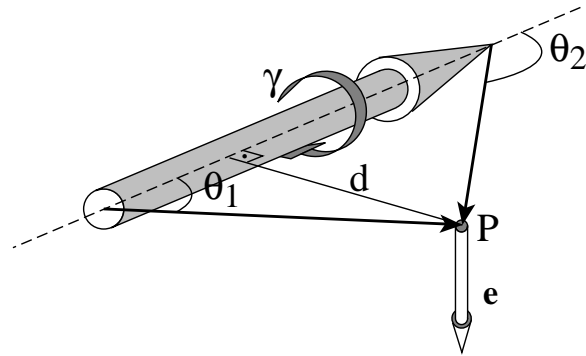


Figure 2.3: Finite Segment of a Straight Vortex Filament

that linearly connect the corner points of each “ring” as shown in Figure 2.3, where  $\mathbf{e}$  is the unit velocity vector perpendicular to the plane spanned by the lattice segment and the vector along  $d$ . The Biot-Savart law for the straight vortex filaments of the lattice has the following form, see Karamcheti [42]:

$$\mathbf{v}(P) = \mathbf{e} \frac{\gamma}{4\pi d} (\cos\theta_1 - \cos\theta_2). \tag{2.24}$$

Equation (2.24) is used in the UVLM to calculate the velocities associated with the vorticity on the body surfaces and in the wakes. The nature of the velocity field created by an individual vortex filament is depicted in Figure 2.4. It is evident, that implementation of

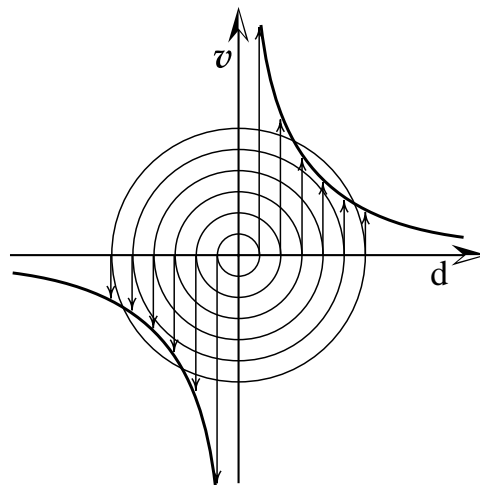


Figure 2.4: Velocity Field Induced by Vortex Filament

Equation (2.24) requires special treatment in case the perpendicular distance of the point of interest to the active vortex segment,  $d$ , approaches zero. This scenario and its implications is discussed in Chapter 2.2.4.

## 2.2.4 Working with Singularities

In general there are two different types of singularities that occur upon application of Equation (2.24):

1. free wake — bound wake singularities
2. free wake — free wake singularities

When vorticity is shed from an edge of a body into the wake, under certain circumstances, these wake panels can end up in close proximity to body panels. This is most likely to take place when vortex roll-up occurs along the wing tip, when a free wake forms close to another body's surface, or when leading-edge separation is modeled; the latter is of no concern to this work. By the same token, when multibody configurations are modeled using the UVLM, it is inevitable that free wakes coming from the different bodies will pass close to each other as they are convected downstream.

In such situations the distance  $d$  from a lattice segment to the point of induced velocity, as depicted in Figure 2.3, can become very small, resulting in inadmissibly large velocity contributions from this segment. Such high contributions due to the close proximity of potential vorticities can cause the solution to diverge. As a consequence, all vortex-lattice methods use some kind of “cutoff distance” that limits the influence of such vortex segments. According to Seginer et al. [69] there exist three “cutoff” methods: a “viscous-core” (solid-body rotation or “eddy” (see Karamcheti [42]) can be added to every vortex, a constant induced velocity can be employed, or two vortices can be combined into one when they are too close. Combining vortex segments that are too close to each other is fairly difficult to implement and increases book-keeping efforts significantly. In light of the fact that computation time is of the essence and that Preidikman [59] obtained good results for his multibody configurations by using a core-cutoff approach, the choice was between the “eddy” and the core of constant velocity.

An “eddy” is characterized by a circulatory flow with constant vorticity inside its core and a circulatory flow without rotation outside its core. In other words, inside the core  $v_\theta \sim r$  and outside  $v_\theta \sim 1/r$ . Figure 2.5 shows the velocity field induced by such a “viscous-core” vortex. It has one advantage over the “constant velocity” core-method: the acceleration field is continuous. A discontinuity in the acceleration can have disrupting effects on the wake.

In either case, specifying the cutoff distance is based on empirical considerations and has no theoretical basis or justification. As a result the solution is no longer unique and depends on the designated cutoff distance. Consolation comes from the fact that small variations in the shapes of the free wakes have little impact on the overall solution — still the physics of the results must always be questioned. From the experimental analysis by Rusak et al. [67] a good range for the cutoff distance is between 10% and 25% of the smaller of the panel dimensions. The vortex participation is not fully accounted for above the upper bound and

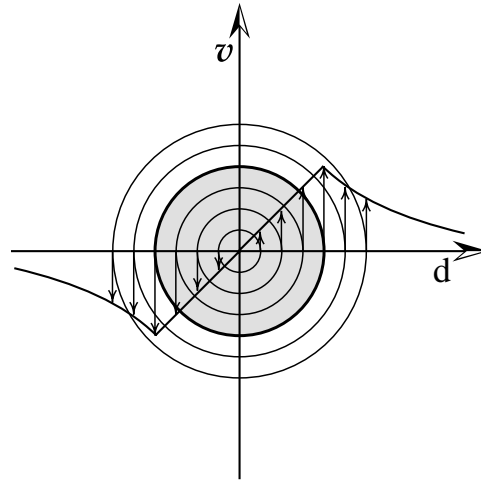


Figure 2.5: “Viscous-Core” Vortex Velocity Field

the induced velocities are too strong and may cause the solution to diverge below the lower bound. A small cutoff distance may also generate large local pressure variations on the surface of the body in the proximity of a free vortex.

The cutoff method employed in this work is based on the “eddy”, where the viscous core (twice the cutoff distance) has been set to 30% of the length of the active lattice segment. Choosing the length of the active segment rather than the smallest of panel dimensions improved stability along adjacent body wakes, i.e., pylon vs. wing and pylon vs. store, where further downstream interwake roll-up between the wing and pylon wake produced panels with high aspect ratios. With the above choice for cutoff, the UVLM generated a smooth vortex roll-up and remained stable under crosswake interference.

### 2.2.5 Wake Development

The wake is an essential part of the UVLM. It is a consequence of satisfying the Kutta condition by employing the theorems of Helmholtz and Kelvin. It is also responsible for the flow being history-dependent.

Helmholtz’s theorem states that in an inviscid and irrotational flow, “the outflow of vorticity through any surface element moving with the fluid remains a constant for all times.” Together with Kelvin’s theorem of “conservation of circulation,” which in mathematical terms is equivalent to Helmholtz’s theorem but is stated in terms of circulation, it formulates the basis for the wake-shedding procedure utilized in the UVLM.

To satisfy the conservation requirement, vorticity is shed from the trailing edges of the bodies into the wake. When a vortex panel has entered the wake it will retain its strength for all

times, i.e.,  $(D\gamma/Dt) = 0$  as required by Helmholtz's theorem. Wake panels are convected smoothly through the local particle velocities such that the vortex lines follow streaklines from the shedding point into the far wake. Very much like a film that rolls off a reel, the wake is shifted into the flow row by row, thus forming the trailing free vortex. With that, the wake "counter balances" the strengths of the bound vortices and ensures that Kelvin's circulation theorem is always satisfied. In fact, this procedure of wake shedding implicitly satisfies the Kutta condition. Kutta's condition on flow past an airfoil formulated in 1902 states that "the circulation set up around an airfoil be of a strength just sufficient to make the flow leave the airfoil smoothly at the trailing edge." The UVLM accomplishes this by convecting wake elements with local particle velocities and consequently rendering the wake force free.

There are various options for calculating the path of wake particles, and efforts have been made in the past to contrast different methods. It has been found that a simple first-order Euler integration provides sufficient accuracy and requires the least computational cost. The difference between converged solutions is too small to justify application of a more costly method (see Seginer et al. [69]). The Euler integration scheme implemented here is

$$\mathbf{r}_i(t) = \mathbf{r}_{i-1}(t - \Delta t) + \mathbf{v}(\mathbf{r}_{i-1}(t - \Delta t), t) \Delta t \quad (2.25)$$

where  $\mathbf{r}(t)$  is the position of a given particle and is calculated by convecting the downstream end points of segment  $i - 1$  found at the previous time step. The only exception to this rule is at the trailing edge of the body, where the wake will always stay attached, i.e., the upstream edge of the wake will always coincide with the trailing edge of the body.

### 2.2.6 The Unsteady Bernoulli Equation

The UVLM uses the unsteady Bernoulli equation to obtain the pressures at the control points of the bodies. Recalling Equation (2.17),

$$\frac{\partial \phi}{\partial t} + \frac{p}{\rho} + \frac{1}{2}v_j v_j = \text{const.},$$

and rewriting it in terms of a differential between a point on the body  $i$  and a point in the far field lying on the same streamline, one can define the pressure coefficient  $(C_p)_i$  as follows:

$$\begin{aligned} p_i &= p_\infty + \frac{1}{2}\rho V_\infty^2 \left[ 1 - \left( \frac{v_i}{V_\infty} \right)^2 \right] - \rho \frac{\partial \phi_i}{\partial t} \\ (C_p)_i &= 1 - \left( \frac{v_i}{V_\infty} \right)^2 - \frac{2}{V_\infty^2} \frac{\partial \phi_i}{\partial t}, \end{aligned} \quad (2.26)$$

where

$$(C_p)_i = \frac{p_i - p_\infty}{\frac{1}{2}\rho V_\infty^2}.$$

Calculating the velocities at point  $i$  of interest can be accomplished in fairly straightforward manner by application of the Biot-Savart law. However, there is an inherent difference in the treatment between bodies of zero thickness and those of finite thickness. Also, the evaluation of the unsteady portion of the equation, represented by  $\partial\phi_i/\partial t$ , involves some algebraic manipulations that may not be obvious to the reader. The procedures will therefore be discussed in detail. For convenience of writing, the index  $i$  is dropped, with the understanding that all following quantities are computed at a particular control point  $i$  on the body.

### Bodies of Zero Thickness

For bodies of zero thickness, the vorticity inside the bound surface is proportional to the velocity jump across that surface. Rather than calculating upper and lower parameters (velocity, velocity potential, pressure, and force) explicitly, it is useful to express all quantities in terms of relative values, i.e., as the difference between their upper and lower-surface values. The net-pressure coefficient assumes the form

$$\Delta C_p = \underbrace{\left[ \left( \frac{v}{V_\infty} \right)_u^2 - \left( \frac{v}{V_\infty} \right)_l^2 \right]}_{\Delta C_{p_{ss}}} + \frac{2}{V_\infty^2} \underbrace{\left[ \left. \frac{\partial\phi}{\partial t} \right|_u - \left. \frac{\partial\phi}{\partial t} \right|_l \right]}_{\Delta C_{p_{us}}}, \quad (2.27)$$

where steady,  $\Delta C_{p_{ss}}$ , and unsteady portions,  $\Delta C_{p_{us}}$ , are identified by the horizontal braces. To further improve readability,  $(\mathbf{v}/V_\infty)$  will be replaced by  $\mathbf{v}$ , a nondimensional velocity.

First, to derive the steady net-pressure coefficient, the steady-state portion of Equation (2.27) is modified as follows:

$$\begin{aligned} \Delta C_{p_{ss}} &= v_u^2 - v_l^2 = (\mathbf{v}_u + \mathbf{v}_l) \cdot (\mathbf{v}_u - \mathbf{v}_l) \\ &= 2\mathbf{v}_m \cdot \Delta\mathbf{v}, \end{aligned} \quad (2.28)$$

with  $\mathbf{v}_m = (1/2)(\mathbf{v}_u + \mathbf{v}_l)$  and  $\Delta\mathbf{v} = \mathbf{v}_u - \mathbf{v}_l$ . This representation is advantageous for calculating the net-pressure coefficient and has a sound foundation in the physical interaction of vorticity and freestream. Figure 2.6 displays the principle of this interaction for the simple case of a two-dimensional panel. The thickness of the panel is displayed only for conceptual purposes. Velocity  $\mathbf{v}_m$  is the normalized mean velocity at the control point, which is the sum of all normalized induced velocities; it is the dimensional equivalent of  $\mathbf{v}_{mean}$  from Equation (2.21). The relative velocity jump across the bound vortex of the surface is represented solely by  $\Delta\mathbf{v}$ , which consequently adds only an in-plane component to the mean velocity at the control point. To calculate  $\Delta\mathbf{v}$ , the panel-bounding vortex segments (two in Figure 2.6) are combined into one resultant segment at the control point. The velocity difference across a panel surface is finally obtained by dividing the resultant vortex segment by the panel area (panel length in Figure 2.6). Velocities  $\Delta\mathbf{v}$  are thereby average values over the panel dimensions.

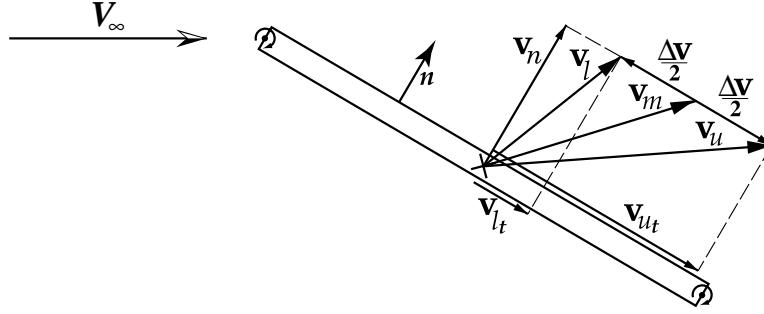


Figure 2.6: Velocities at Control Point

Calculation of the unsteady portion of Equation (2.27) involves determining the rate of change of the velocity potential  $\phi$  with respect to the NR frame. The partial derivative is approximated through the first-order forward difference

$$\frac{\partial \phi}{\partial t} \simeq \frac{\phi(\mathbf{r}, t + \Delta t) - \phi(\mathbf{r}, t)}{\Delta t}, \quad (2.29)$$

which expresses the rate of change of  $\phi$  at a fixed point in space. The finite difference of Equation 2.29 is difficult to obtain, and it is a typical procedure to exchange the above equation for an equivalent relationship that involves the rate of change of  $\phi$  at a fixed point on the moving body. By expanding the term  $\phi(\mathbf{r} + \Delta \mathbf{r}, t + \Delta t)$  through a Taylor series and neglecting higher order terms, it is a straightforward matter to derive the relationship

$$\frac{\partial \phi}{\partial t} \simeq \frac{\phi(\mathbf{r} + \Delta \mathbf{r}, t + \Delta t) - \phi(\mathbf{r}, t)}{\Delta t} - \nabla \phi \cdot \left( \frac{\Delta \mathbf{r}}{\Delta t} \right).$$

The finite difference part of above equation is essentially the total derivative of  $\phi(\mathbf{r}, t)$  following a fixed point on the moving body, and  $(\Delta \mathbf{r}/\Delta t)$  is chosen to be the velocity at a control point expressed in terms of the NR frame, i.e.,

$$\begin{aligned} \frac{\partial \phi}{\partial t} &\simeq \frac{D\phi}{Dt} - \mathbf{v} \cdot \mathbf{v}_{CP} \\ &\simeq \frac{D\phi}{Dt} - \mathbf{v} \cdot (\mathbf{v}_{CP}^* - \mathbf{V}_\infty). \end{aligned} \quad (2.30)$$

Upon substitution of Equation (2.30) into the second part of Equation (2.27), an approximate representation for the unsteady net-pressure coefficient is obtained:

$$\begin{aligned} \Delta C_{pus} &= \frac{2}{V_\infty^2} \left[ \left. \frac{D\phi}{Dt} \right|_u - \left. \frac{D\phi}{Dt} \right|_l \right] - 2(\mathbf{v}_{CP}^* - \mathbf{v}_{FS}) \cdot (\mathbf{v}_u - \mathbf{v}_l) \\ &\simeq \frac{2}{V_\infty^2 \Delta t} \left[ \left( \phi_u(t) - \phi_l(t) \right) - \left( \phi_u(t - \Delta t) - \phi_l(t - \Delta t) \right) \right] + \\ &\quad - 2\Delta \mathbf{v} \cdot (\mathbf{v}_{CP}^* - \mathbf{v}_{FS}), \end{aligned} \quad (2.31)$$

where  $\mathbf{v}_{FS} = (\mathbf{V}_\infty/V_\infty)$ . To calculate the differences in  $\phi$  across the panel surface in Equation (2.31), the definition of the velocity potential,  $\mathbf{v} = \nabla\phi$ , is manipulated to state  $d\phi = \mathbf{v} \cdot d\mathbf{l}$  or

$$\phi_u - \phi_l = \int_{l_l}^{l_u} \mathbf{v} \cdot d\mathbf{l} . \quad (2.32)$$

Because the bodies that are considered here are of zero thickness, the integration of Equation (2.32) is, in fact, along a closed path. By use of the definition of circulation,

$$\Gamma = \oint_c \mathbf{v} \cdot d\mathbf{l} ,$$

the value of the integral of Equation (2.32) is equal to the circulation associated with the vorticity encircled by that path. For the discrete case of the vortex-lattice bodies, the total circulation is simply the summation of individual strengths of the vortex segments encountered along the path of integration, weighted by the angle the lattice segment makes with the path of integration:

$$\int_{l_l}^{l_u} \mathbf{v} \cdot d\mathbf{l} = \sum_j \gamma_j \cdot \mathbf{n}_j . \quad (2.33)$$

A full contribution of a lattice segment to the total circulation is only possible if its orientation in space is exactly perpendicular to the path of integration. Recalling the relationship between  $\gamma$  and the strength of the panel vorticity  $G$  from Section 2.2.2, it is easy to show that the net value of the velocity potential at any panel simply equals the strength of the panel vortex itself times the sweep angle of the active panel, i.e.,  $\phi_u - \phi_l = G \cos(\alpha)$ . The total net-pressure coefficient for bodies of zero thickness is thus given by

$$\Delta C_p \simeq 2\Delta\mathbf{v} \cdot (\mathbf{v}_m + \mathbf{v}_{FS} - \mathbf{v}_{CP}^*) + \frac{2}{V_\infty^2 \Delta t} (G(t) - G(t - \Delta t)) \cos(\alpha) . \quad (2.34)$$

Figure 2.7 shows as an example of how the procedure works for the simple case of a two-dimensional body and  $\cos(\alpha) = 1$ . Calculating the net value of the velocity potential at control point  $i = 3$  amounts to a summation of segment strengths  $\gamma_1$  through  $\gamma_3$ , which is equal to  $G_3$ , i.e.,

$$\phi_u - \phi_l = \gamma_1 + \gamma_2 + \gamma_3 = G_3 .$$

### Bodies of Finite Thickness

Bodies of finite thickness cannot take advantage of the “net-difference methods” developed above to calculate surface net-pressures. It is necessary to formulate equations in terms of

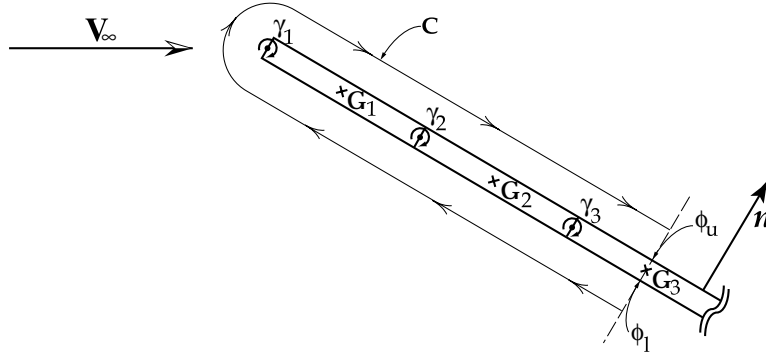


Figure 2.7: Net-Value of the Velocity Potential Through Integration

absolute “upper” surface quantities, i.e.,  $\mathbf{v}_u$  and  $\phi_u$ . On the “lower” surface, which is in fact inside the body, the velocities are by definition zero. As a result, the steady-state portion of  $C_p$  from Equation (2.26) is given by

$$C_{p_{ss}} = 1 - \left( \frac{V}{V_\infty} \right)^2 = 1 - v_u^2,$$

where  $\mathbf{v}_u$  is  $(\mathbf{V}/V_\infty)$ . Since calculating velocities at control points is not fundamentally different from that for bodies of zero thickness,  $\mathbf{v}_u$  as well as  $\mathbf{v}_l$  can be expressed in terms of  $\mathbf{v}_m$  and  $\Delta\mathbf{v}$ :  $\mathbf{v}_u = \mathbf{v}_m + (\Delta\mathbf{v}/2)$  and  $\mathbf{v}_l = \mathbf{v}_m - (\Delta\mathbf{v}/2)$ . Since the lower-surface velocities must be zero, it follows that  $\mathbf{v}_m$  and  $(\Delta\mathbf{v}/2)$  are equal. For computational reasons the steady-state pressure is expressed as a function of both  $\mathbf{v}_m$  and  $\Delta\mathbf{v}$ , yielding

$$C_{p_{ss}} = 1 - 2\Delta\mathbf{v} \cdot \mathbf{v}_m. \quad (2.35)$$

The unsteady portion of Equation (2.26) is again formulated in the NR frame and is transformed in the exact same manner as explained for bodies of zero thickness. As a result, the term  $(D\phi/Dt)$  is obtained, which requires calculation of the rate of change of  $\phi$  at a point on the moving surface. To accomplish this, it is easiest to pick a point in the far field where  $\phi$  is known and does not change with time and to integrate along a straight line to the control point of one designated surface panel. Once the value of  $\phi$  is known for one panel on the surface, the path of integration continues from this panel over the surface to all other panels — where every panel need be touched only once. This utilizes Equation (2.32),

$$\phi_{i+1} = \phi_i + \int_{l_i}^{l_{i+1}} \mathbf{v} \cdot d\mathbf{l}, \quad (2.36)$$

with  $l_l = l_i$  and  $l_u = l_{i+1}$ , where  $i = 0, 1, 2, \dots, N$ . At  $i = 0$  the integration starts in the far field with  $v(l_0) = V_\infty$  and  $\phi_0 = \phi_\infty$ , and  $N$  is the total number of surface panels. For any other value of  $i$ , the integration stays on the body’s surface and works its way successively

from panel to panel. Finally the rate of change of  $\phi$  is approximated by the backward difference between the current value and the previous value in time. The path of integration over the surface of the body changes as a function of the body's motion, which means that the path of integration must be newly determined for every step in time, though it always begins at the same point in space.

Finally, Equation (2.35) together with a backward difference approximation for  $(D\phi/Dt)$  yields the total surface pressure on a body of finite thickness,

$$C_p \simeq 1 - 2\Delta\mathbf{v} \cdot (\mathbf{v}_m + \mathbf{v}_{FS} - \mathbf{v}_{CP}^*) + \frac{2}{V_\infty^2} \left[ \frac{\phi(t) - \phi(t - \Delta t)}{\Delta t} \right]. \quad (2.37)$$

# Chapter 3

## Numerical Model

### 3.1 Structure

#### 3.1.1 ABAQUS/Standard

The development of a versatile nonlinear aeroelastic analysis tool is the goal of this research, and ABAQUS is the ideal candidate to meet this goal. ABAQUS/Standard is a commercial finite element code that derives its success from its reputation of reliability and robustness in nonlinear FEM analysis. It offers the desired flexibility to tailor the numerical model to a more realistic description of the real structure, offering a variety of common nonlinear components in aeroelasticity, such as free play, Coulomb friction, and nonlinear elasticity. The element and material libraries are extensive and allow hybrid element formulations, where standard elements can be modified by the user, to the extent of fully user defined elements; piezoelectric materials can also be modeled in ABAQUS.

ABAQUS provides user programmable interfaces, so-called USER SUBROUTINES, to manipulate internal data as well as to communicate with external processes. User subroutines operate like standard FORTRAN subroutines and are called by ABAQUS during an analysis when certain conditions (defined by ABAQUS) are met. Each subroutine serves a particular purpose and handles a different set of solution or model variables. The user is free, within certain limits, to implement FORTRAN code into these routines that now become a part of the overall analysis.

Within one simulation, it is possible to successively exercise different analysis types. For example a static analysis can precede a dynamic analysis in one run. This is particularly helpful for determining the steady-state solution at a particular airspeed of the aeroelastic model under investigation as explained in Section 4.3.

The following section presents the details of the ABAQUS model for the F16 configuration

analyzed in this research.

### 3.1.2 The Structural Model

The structural model used here is a parametric representation of a symmetric, full-scale, semispan fuselage-section/wing/pylon/store model of an F16 aircraft. The model is based on an F16 configuration investigated by Cazier and Kehoe [10, 9, 11, 8] and others, e.g., Mignolet et al. [49], which includes a wing-tip missile, a GBU-8/B weapon at span station 3 m, and a half-full 1400 lit fuel tank at span station 1.8 m. This configuration experiences 5.1 Hz limited amplitude flutter oscillations at Mach numbers above 0.70.

During the research for structural properties it became evident that exact specifications are classified as “sensitive information.” This made it necessary to restrict the model design to available data and dampened the prospects of achieving accurate resemblance of the real structure. Hence, the data used here to define the structural model are a conglomerate of properties collected from various publications that were publicly accessible. Figure A.2 in the Appendix displays a schematic of the structural dimensions of the wing/pylon/store part of the parametric model under investigation. Fuel-tank and wing-tip missile are omitted because sufficient information to model these components was not available.

With ABAQUS as a host environment, it would be a reasonably easy task to adapt the FEM model should more in-depth structural data become available. In the following the individual bodies of the employed model will be discussed in detail.

#### Fuselage-Model

The fuselage-section model does not serve a structural purpose at this time. It is incorporated for aerodynamic reasons and assumes the function of completing the symmetry of the model. Its rectangular shape is made of thirty three-dimensional massless rigid surface elements<sup>1</sup>; the wing root connects on one side and the opposite side is clamped to the plane of symmetry. The dimensions are determined by the overall span minus the wing-span of the F16 and the length of the in-board chord section of the wing. Length and width of the fuselage section are thus 4.13 m  $\times$  1.355 m.

#### Wing-Model

The wing planform of the F16 is effectively that of a cropped delta wing with a 40 degree leading-edge sweep. Its body incorporates eleven spars and five ribs with an airfoil section of a four percent thickness-to-chord ratio. The root section of the wing blends with the

---

<sup>1</sup>ABAQUS notation: R3D4

fuselage, making it impossible to tell where the wing begins and the fuselage ends. The wing thickness increases gradually in the region of the root resulting in a stiffer wing over conventional designs. The total mass of the wing is approximately 2000 kg, Reed et al. [63, 62].

Lacking structural details of the wing, it was decided to model it as a plate of isotropic, linear-elastic properties with the dimensions of the F16 wing's planform and linearly decreasing plate-thickness (taper) along the span from the root to the pylon station, i.e., span station 3 m. The plate is made relatively thick in the region of the root in order to increase the stiffness in that region. From here, the plate tapers off to the thickness at span station 3 m and then maintains a constant thickness all the way out to the wing tip. General purpose, four-noded, quadrilateral, doubly-curved shell elements<sup>2</sup> are employed to discretize the plate. The shell elements have 24 active degrees of freedom (DOFs); three translational and three rotational DOFs at each of four nodes. The plate nodes along the root chord are pinned one-to-one to their corresponding fuselage nodes with the exception of the three downstream nodes along the inboard edge of the flaperon. This region does not contribute to the root-stiffness of the wing.

## Pylon Model

The Pylon is modeled as a rigid surface of zero thickness with all inertia effects concentrated at a lumped mass of 161 kg at the centroid. Its upper edge is rigidly attached to the wing at span station 3.0 m by two zero-length rigid beam elements. The lower edge accommodates the store pivot point or joint about which the store can exercise pitch and yaw degrees of freedom. At the pivot point, the lower edge of the pylon makes a  $\pm 5$  degree angle with the horizontal in order to enable the store to undergo the same amount of "free" pitch before the rigid bodies of store and pylon make contact. In Figure A.2 the grey shaded area depicts the shape of the FEM pylon model. Both pivot DOFs are restrained by torsional springs where the pitch stiffness can be adjusted to model both "rigid" and flexible pylon models listed in Table 3.2; the yaw stiffness is fixed at  $1.85 \text{ kN} \cdot \text{m}/\text{rad}$ .

## Store Model

The store model is based on the GBU-8/B weapon, which is suspended from the wing-mounted pylon at span station 3.0 m. It is modeled as a rigid body of revolution using 420 rigid four-noded three-dimensional elements<sup>3</sup>. The inertia data is summarized in Table 3.1. The store model is suspended from the pylon pivot point right above its own center of gravity (see Figure A.2).

---

<sup>2</sup>ABAQUS notation: S4

<sup>3</sup>ABAQUS notation: R3D4

Table 3.1: Store Model Inertia Properties.

Property	Value
Mass [kg]	1027.50
$I_{\text{pitch}} + I_{\text{yaw}}$ [kg · m <sup>2</sup> ] about C.G.	710.50
$I_{\text{roll}}$ [kg · m <sup>2</sup> ] about C.G.	27.52

### Combined Wing/Pylon/Store Model

As mentioned above, the structural model is intended to represent the flutter-prone F16 configuration examined by Reed, Cazier, Foughner and others as closely as available data allows. Table 3.2 displays the natural frequencies of a configured F16 wing obtained through ground vibration tests by Cazier and Kehoe [9, 11]. In the case of the production pylon,

Table 3.2: Symmetric Mode Frequencies.

	F <sub>1</sub> [Hz]	F <sub>2</sub> [Hz]	F <sub>3</sub> [Hz]	F <sub>4</sub> [Hz]	F <sub>5</sub> [Hz]
PP <sub>GVT</sub>	4.07 <sub>h<sub>1</sub></sub>	5.35 <sub>α+θ</sub>	8.12 <sub>γ</sub>	12.28 <sub>h<sub>2</sub></sub>	-
DP <sub>GVT</sub>	3.31 <sub>α</sub>	3.95 <sub>h<sub>1</sub></sub>	9.64 <sub>h<sub>2</sub></sub>	-	-
DP <sub>A</sub>	3.26 <sub>α</sub>	3.69 <sub>h<sub>1</sub></sub>	5.31 <sub>γ</sub>	6.0 <sub>θ</sub>	9.98 <sub>h<sub>2</sub></sub>

PP = Production Pylon  
 DP = Decoupler Pylon  
 GVT = Ground Vibration Test  
 A = FEM Analysis

$\alpha$  = Store Pitch  
 $\gamma$  = Store Yaw  
 $\theta$  = Wing Torsion  
 $h_i$  = *i*th Wing Bending

which is commonly referred to as rigid pylon in the literature, store pitch and wing torsion are coupled together and appear as one mode. When the decoupler pylon is activated, the store-pitch mode decouples from the wing torsion and falls below the fundamental wing-bending frequency. Cazier's papers do not contain experimental data on the effects of the decoupler pylon on the wing-torsion frequency, other than results from FEM analysis.

An ad-hoc model updating procedure was employed to match the natural frequencies of the FEM model to the measured values of the F16. The material properties of the numerical wing plate, such as Young's modulus, density, and shell thicknesses, were determined empirically through trial and error. Material properties of real metals as well as deflection behavior under static loads guided the search for admissible material strengths and properties. Table

3.3 displays the material properties as chosen for this wing model. Row five displays the shell

Table 3.3: Wing Model Material Properties.

Property	Value
E [GPa]	115
G [GPa]	46
$\nu$	0.25
$\rho$ [ $\frac{\text{kg}}{\text{m}^3}$ ]	4730
t [m]	0.075, 0.03, 0.03
m [kg]	2078

thicknesses at the root, pylon station, and wing tip, respectively. The natural frequencies for the clamped-symmetric mode shapes of the model together with the required spring stiffnesses for store pitch are summarized in Table 3.4. The respective mode shapes are displayed in Figures A.3 and A.4 of Appendix A. There are three categories of interest:

Table 3.4: Clamped-Symmetric Mode Frequencies.

	$K_\alpha$ [ $\frac{\text{kN}\cdot\text{m}}{\text{rad}}$ ]	$F_1$ [Hz]	$F_2$ [Hz]	$F_3$ [Hz]	$F_4$ [Hz]	$F_5$ [Hz]
CW	n/a	$5.3_{h_1}$	$16.04_\theta$	$17.58_{h_2}$	-	-
PP	2800	$3.98_{h_1}$	$5.36_{\alpha+\theta}$	$8.12_\gamma$	$10.74_{h_2+\alpha}$	$12.23_{\theta_{WT}}$
DP	425	$3.31_\alpha$	$4.00_{h_1}$	$8.12_\gamma$	$9.13_{\theta_{WT}}$	$11.22_{h_2+\theta_{WT}}$

CW = Clean Wing

PP = Production Pylon

DP = Decoupler Pylon

$\alpha$  = Store Pitch

$\gamma$  = Store Yaw

$\theta$  = Wing Torsion

$\theta_{WT}$  = Wing-Tip Torsion

$h_i$  =  $i$ th wing bending

clean wing (CW), “rigidly” connected Store (PP), and elastically connected store (DP). It is clearly noticeable, how the external store decreases both bending and torsion frequencies of the clean wing, the latter of which is affected more significantly. In the case of the production pylon, the torsion and store-pitch frequency collapse to one mode, drastically reducing the bending-torsion ratio of this model from  $\theta/h_1 = 3.0$  down to  $\theta/h_1 = 1.4$ . This means, that the bending-torsion frequency separation of the clean wing is reduced by a factor of 53%. The decoupler pylon partially reestablishes the spread between wing bending and torsion to  $\theta_{WT}/h_1 = 2.3$ , i.e., an increase of 39% over the PP case. These predictions are in good qualitative agreement with Reed et al. [63] on decoupler pylon wing/store interaction.

Modes one and two of the PP and DP models trade places as the stiffness of the pylon changes from “rigid” to soft. The store-pitch mode drops below the fundamental bending mode and is freed of any wing mode participation. The fundamental bending mode displays a very small increase in modal frequency as the pylon is reduced in stiffness.

The third mode of both pylon configurations is easily identified as store yaw. This mode does not involve any wing participation and does not recognize the change in pylon pitch stiffness.

Mode five of the stiff pylon configuration and mode four of the soft pylon configuration are best characterized as wing-tip-torsion modes. In fact, they are almost identical in shape and differ only in their corresponding modal frequencies. Case PP exhibits a noticeably higher wing-tip-torsion frequency than case DP, which can be attributed to the presence of a stiff versus a soft pylon. A “rigid” pylon stiffens the “root” of the wing tip along the pylon station, resulting in higher frequencies over the softer decoupler pylon.

Mode four of the stiff pylon and mode five of the soft pylon both exhibit second-bending characteristics. In case PP, the bending motion is very pronounced and is accompanied by store-pitch motion. In case DP, the second bending mode is overlaid by wing-tip torsion, which makes it difficult to identify the nature of the mode. It is worth noting, that the natural frequencies of the first and second bending modes decrease significantly upon adding an external store but the softening of the pylon stiffness results in a small but noticeable frequency increase.

Excellent agreement of frequencies between the numerical model and the measured frequencies can be observed, as can be verified through comparison of Tables 3.4 and 3.2.

## 3.2 The Aerodynamic Model

Just like the structural model, the aerodynamic model consists of the fuselage, wing, pylon, and store, with a total of 632 panels and 748 nodes. The fuselage (40 panels), wing (160 panels), and pylon (52 panels) are modeled as bodies of zero thickness and zero camber. Here the UVLM models only the velocity discontinuity that builds up between the lower and upper surfaces of the bodies. The store (420 panels) is an axisymmetric body of revolution and is conceptually different from the rest of the model. Surface velocities here are absolute values, representing the actual speed of the flow on the upper surface — the flow speed on the lower surface, i.e., inside the body, is in fact zero. All solution variables of the semispan model are obtained at the panel control points which are located at the panel centroids.

### The Lifting Surface

The aerodynamic characteristics of the lifting-surface wing model are depicted in Figure 3.1. The linear and symmetric (with respect to zero angle of attack) character of the lift

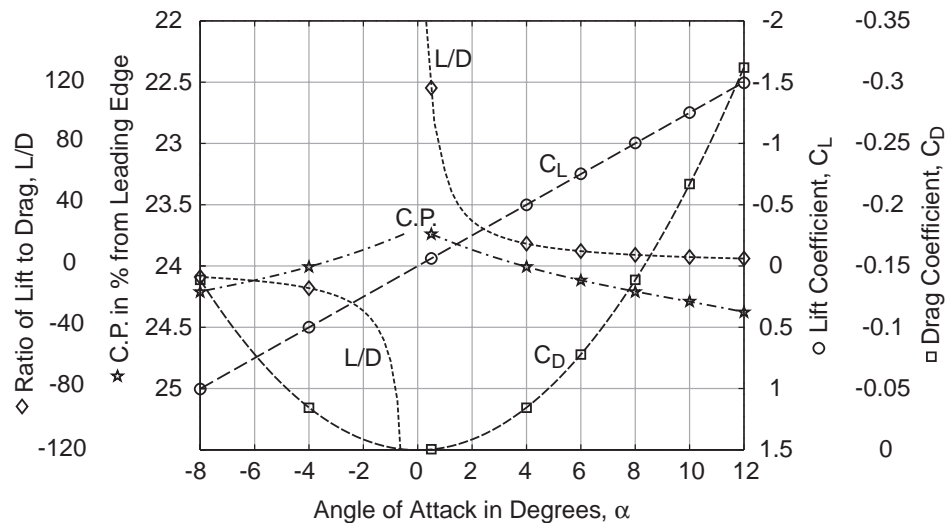


Figure 3.1: Flat Plate Wing Model Characteristics

coefficient,  $C_L$ , is typical of zero thickness and zero camber ideal fluid models and is well represented here. The drag coefficient,  $C_D$ , which refers to the drag due to lift, is a perfect parabola with its minimum of zero drag at zero angle of attack (AOA). As a result, the ratio of lift to drag assumes the shape of a hyperbola, experiencing its singularity at zero AOA. This is a purely numerical characteristic and simply verifies the inviscid nature of the flow past a body of zero thickness. It states that drag modeled here is exclusively due to the production of lift.

The center of pressure, C.P., remains in the neighborhood of the quarter chord location over the above range of angle-of-attack values. This quantity, which reflects the point of application of resultant forces, is more sensitive to AOA variations when camber is present. For small cambers the relative pressure distribution along the chord does not change much with angle of attack, keeping the C.P. fairly steady.

Over the displayed range of angle-of-attack values, the proposed lifting-surface model demonstrates good predictions of flow phenomena. Flow separation and wake turbulence become prominent factors at larger angles of attack, making it necessary to refer to a more indepth flow representation.

It is difficult to quantify how well the presented model can predict the aerodynamic characteristics of the F16 wing. In light of the F16's supersonic operation envelope, it is reasonable

ot assume that the wing camber of its wing is, in fact, small and may be reasonably well represented by a flat plate model.

### The Store Model

The store body is modeled as an axisymmetric bluff body with an open aft body from which the wake is shed. All surface panels are defined to maintain an aspect ratio close to unity. The aerodynamic characteristics of the store model are depicted in Figure 3.2. The forces and moments in Figure 3.2 are calculated with respect to the store pivot point versus angle of attack. In this case the AOA is measured between the freestream and the angle of incidence of the rigid fuselage. It is interesting to note that the store is subjected to

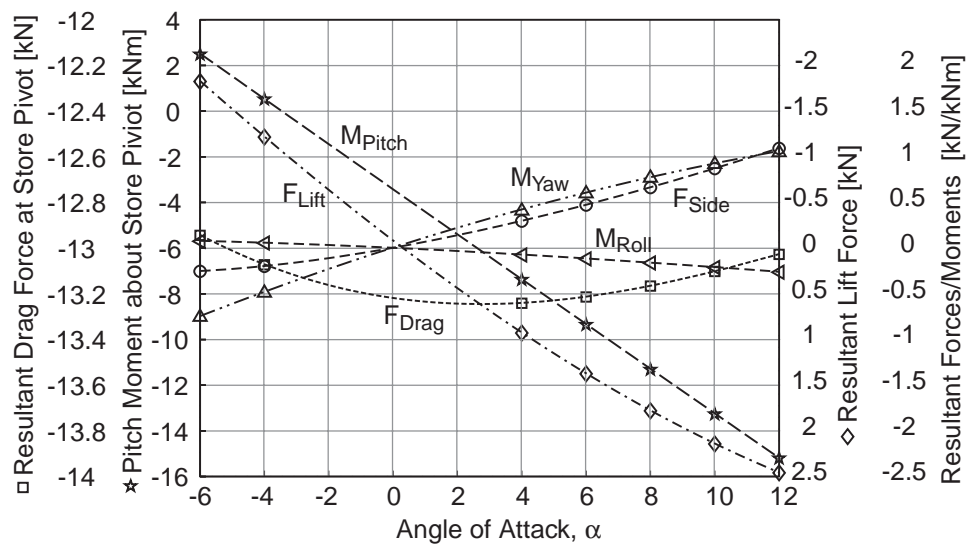


Figure 3.2: Bluff Store Model Characteristics

permanent drag force that has a nonzero minimum at an AOA larger than zero. Because the aft body is open, the pressures on the bluff forebody (nose) generate uncompensated force components in the direction of the freestream, i.e., drag. This drag force reaches its smallest value between 2 and 3 degrees AOA, when the forebody assumes an angle to the freestream that minimizes the pressure induced downstream force components on the forebody. The drag force produces a nose-down pitch moment about the pivot point as long as its line of action falls below the pivot. At about  $-3.5^\circ$  the pitch moment reaches zero and for angles below  $-3.5^\circ$  the resultant drag force induces a nose-up pitch moment. Under steady-state conditions the predicted pitch-up moment at  $12^\circ$  AOA will result in store-pitch motion of

2.15° up for the soft pylon and 0.33° up for the stiff pylon. In general, the resultant drag force and pitch moment dominate the store behavior, all other forces and moments are relatively insignificant. A small lift and side force can be observed accompanied by small roll and yaw moments. These are a result of locally accelerated flow over the nose cone producing small but nonzero net pressures laterally and transversely.

# Chapter 4

## Aeroelasticity

### 4.1 Equation of Motion

The equation of motion of the complete aeroelastic wing-model is expressed in terms of a body-fixed coordinate frame that is attached to the airplane and translates, as the airplane “flies”, through a Newtonian reference frame at a constant speed of  $V_\infty$ . It consists of two parts: the structure on the left-hand-side and the aerodynamic load vector on the right-hand-side. In the case under consideration, the structural model is a linear-elastic plate, two rigid bodies, and a 2 DOF elastic joint that is constrained by a linear torsional spring in both DOFs, respectively. The plate model has 187 nodes of which 8 are clamped along the root and an additional 2 are constrained through a rigid link along the pylon interface. All together, the structural model consists of  $178 \times 6 + 2 = 1058$  DOF.

The air loads that constitute the load vector are defined by means of the unsteady Bernoulli equation which is a function of panel control-point positions, velocities, and accelerations all of which are derived from corresponding nodal quantities. Pressures at control points are defined to be constant over the panel surface and are applied as panelwise distributed pressure loads to the structure. The aerodynamic model, thereby, has one DOF per panel or a total of 632 DOF.

In general terms, the aeroelastic equation can be stated in the following form,

$$[\mathbf{M}]\ddot{\mathbf{q}} + [\mathbf{K}]\mathbf{q} = \{\mathbf{Q}(\ddot{\mathbf{q}}, \dot{\mathbf{q}}, \mathbf{q})\} \quad (4.1)$$

There is structural coupling between the fundamental modes, i.e., bending, twist, and store pitch as well as aerodynamic coupling. Furthermore it is important to note that the acceleration appears on both sides of the equation, explicitly on the left and implicitly on the right; “there is no way to rearrange the equations so that the acceleration only appears on the left”, Mook and Luton [50].

As a result, the aeroelastic equation of motion is solved iteratively in the time domain. The

numerical method is hosted by ABAQUS and is explained in the following sections.

## 4.2 Handshake

The integration process of the nonlinear aeroelastic equation of motion is controlled entirely by ABAQUS. ABAQUS acts as the master process that controls the UVLM through its iteration and increment scheme, inherent to the nonlinear analytical procedure.

ABAQUS offers through so called USER SUBROUTINES the possibility to interact with process data, internal as well as external to the analysis. User subroutines operate like standard FORTRAN subroutines and are called by ABAQUS during an analysis when certain conditions (defined by ABAQUS) are met. In the case under investigation, it is necessary to transfer data between ABAQUS and the UVLM, in order to establish the force-displacement equilibrium iteratively. The data transferred within every iteration, are the air loads and the nodal coordinates or quadrature point coordinates (see Section DLOAD). Three subroutines are employed to handle the communication between ABAQUS and the UVLM: they are UEXTERNALDB, DLOAD, and URDFIL. Each subroutine is called at different situations during the analysis, and each is programmed to perform a different task as will be explained in detail below.

To synchronize alternating access to the data files between ABAQUS and the UVLM, the handshake mechanism relies on three flag files: “strc.flag”, “aero.flag”, and “data.flag”. These flag files as well as the communication data files are placed in a common directory that is shared by both main processes. When a pressure data file, created by the UVLM, is ready to be accessed by ABAQUS, the UVLM will set the “strc.flag”; by the same token, when a displacement data file is ready to be accessed by the UVLM, ABAQUS will set the “aero.flag”. The flag file “data.flag” is used by ABAQUS to pass current step, increment, and iteration information to the UVLM and is created together with the displacement data file. Whenever either code requires new data input from the partner program, it waits until the correct flag file has been set. Once the proper flag has been detected the data file is read in and immediately processed. This procedure involves a large amount of alternate idle time between the two codes. Unfortunately, the nature of the aeroelastic problem limits the parts of the simulation where both programs can work in parallel.

A flow chart of the complete handshake algorithm is given in Figure A.5 of Appendix A.

### Subroutine UEXTERNALDB

The subroutine UEXTERNALDB is called by ABAQUS at the beginning and end of each analysis and increment. It is used to establish the synchronization between the two codes at the beginning of each new and restarted analysis as well as at the beginning of each increment

during an analysis. The subroutine employs a flag bit, LOP, that identifies the state at which the subroutine has been called by ABAQUS. Based on LOP, the “data.flag” file is set with information that the UVLM uses to determine the state of the analysis. During the iteration sequence UEXTERNALDB is not called and consequently cannot be used to control this part of the analysis.

### Subroutine DLOAD

The subroutine DLOAD is called once for every load integration point of the finite element model whenever the system’s stiffness needs to be (re)calculated. Hence, the routine is also called during the iteration sequence of every increment. Part of the parameters that are passed into the routine are the current load integration point (quadrature point) coordinates. This constitutes the only access to ABAQUS-internal solution data making DLOAD the workhorse of the handshake mechanism.

**Step 1.:** When DLOAD is called for the very first time within a new increment, the handshake is activated and a complete set of current air loads is read into memory. Then DLOAD resumes and successively retrieves the loads from memory for the currently processed element during every individual call until the complete model has been treated. When the DLOAD sequence is complete, the entire set of active air loads has been applied.

**Step 2.:** The next series of DLOAD calls is launched by ABAQUS after the solution to the previously applied loads has been obtained (end of iteration), in order to check for convergence of residuals. The handshake mechanism uses this to read the quadrature point coordinates from DLOAD and to write them into memory. Once all elements have been read in, the handshake makes the coordinate data available to the UVLM. By means of isoparametric extrapolation the UVLM obtains the current nodal positions from the quadrature point locations. During this DLOAD series the loading remains unchanged. New air loads can now be calculated by the UVLM (beginning of UVLM iteration) and can then be retrieved during the next sequence of DLOAD calls.

**Step 3.:** Although the loading did not change during the last two ABAQUS iterations, by default at least one more iteration is required to establish convergence. At the beginning of the next iteration, when ABAQUS launches another sequence of DLOAD calls, the handshake mechanism reads in the new set of air loads from the UVLM during the first DLOAD call. The new loading is then applied element by element through concurrent DLOAD calls.

Steps two and three are repeated until convergence has been established. It is important to note, that every two ABAQUS iterations make for only one UVLM iteration. The simple fact that DLOAD is called once for every quadrature point of the model makes such partial redundancy necessary.

### Subroutine URDFIL

The subroutine URDFIL is called once at the end of each increment and allows the extraction of solution variables from ABAQUS-internal data files. The handshake engages in this routine to access the nodal displacements at the end of a converged iteration sequence and to synchronize the end of the current increment with the UVLM.

## 4.3 Solution in Time

The aeroelastic equation of motion is composed of the structural part, native to ABAQUS, and the aerodynamic part, external to ABAQUS. As the aerodynamic part of the solution is a continuous function of the mesh position and velocities, and in return the structural part of the solution is at the same time a continuous function of the air loads, it is necessary to calculate the overall solution iteratively for every step in time (increment).

By engaging a nonlinear solution process, which comes as a standard feature in ABAQUS, ABAQUS derives the solution through an iterative procedure. Hereby, it forms residuals of force and moment by comparing internal loads at the nodes, which are caused by stresses in the elements that are attached to these nodes, and external loads. At each iteration a correction to the solution variables using the tangent stiffness of the system under the current loading is calculated based on the current residuals. The solution has converged once certain tolerance criteria have been met.

The solution for nonlinear problems is integrated in time using the Hilbert-Hughes-Taylor or  $\alpha$ -method, which is an implicit, unconditionally stable, second order accurate member of the Newmark families of finite-difference methods. The parameter  $\alpha$  introduces numerical damping into the equation which can be helpful in eliminating oscillatory behavior due to numerical imprecisions. The value of  $\alpha$  is set to 0.05, which is also the ABAQUS default and recommended choice.

For the model under investigation, the time step size is, in fact, dictated by the aerodynamic model. To guarantee wake stability, it is necessary to maintain well shaped wake panels of possibly unit aspect ratio that are of similar dimensions as the trailing-edge surface panels from which the wake originates. As a result, the time step size becomes a function of air speed and model panel dimensions. Here, the relationship between  $\Delta t$  and  $V_\infty$  is given by  $\Delta t = 0.24/V_\infty$ , where the velocity is in units of m/s. The factor of proportionality in this equation represents the ratio of the average chord length over the number of panels along the chord.

## Starting the Analysis

The direct dependency between airspeed and time step size requires an impulsive start of the analysis. At time  $t = 0$  the structure is in its undisplaced shape and the aerodynamics are jump started with a velocity step-input. ABAQUS is idle at this time and waits for the initial load input, calculated by the UVLM. The loads are determined at the control points of the undeformed mesh using their positions and velocities with respect to the body-fixed coordinate system and the velocity of the freestream. During the initial time step, the control-point velocities,  $V_{CP}$  are zero. Once the loads have been established, passed to ABAQUS, and applied, ABAQUS will calculate the displacements of the structure using the stiffness of the model. The new mesh position is transferred to the UVLM, the corresponding air loads are calculated and are immediately read back by ABAQUS. There exists now a residual between the original force input and the updated force input, which is recognized by ABAQUS as such and thus the nodal displacements are recalculated. This iteration process will continue until the residuals are small enough to satisfy the tolerance requirements. Now, structure and air loads are in equilibrium and the first time step has been completed.

## Stepping Forward in Time

Upon reaching the force-displacement equilibrium, a new increment is initiated by ABAQUS and a “new increment” signal is passed to the UVLM. This signal causes the UVLM to convect the current set of trailing-edge vorticities into the flow. As a result of the newly formed wake, the load vector of the previously balanced solution changes. These new loads are transferred to ABAQUS, starting the iteration process for the current increment. From here, displacements and loads are successively updated until force and moment residuals are small. The control-point velocities that are necessary to calculate the loads are computed by means of a simple backward-difference between the converged control-point positions of the last increment and their momentary positions at the current iteration. During the iteration procedure wake panels retain their position in the flow, with the exception of those panels connected to a trailing edge. The wake nodes that lie on a trailing edge are kept attached to the body while the new equilibrium is found.

## Wake Contributions

An important consideration of the numerical solution in time is the trade-off between computational cost and accuracy of the solution. It has been found that the largest contributor to computational cost stems from the wake shedding procedure and the calculation of wake induced velocities at surface control points. This is due to the simple fact that the wake grows with time, such that with every new increment the number of wake panels increases by the total number of trailing edge and wing-tip panels. For the model considered here, this amounts to 41 new wake panels per increment. The effect of the changing model size is

depicted in Figure 4.1 for the case of a 100 increment simulation with a step wise developing wake. The time to convect the wake and to calculate its influence on the bodies, as depicted

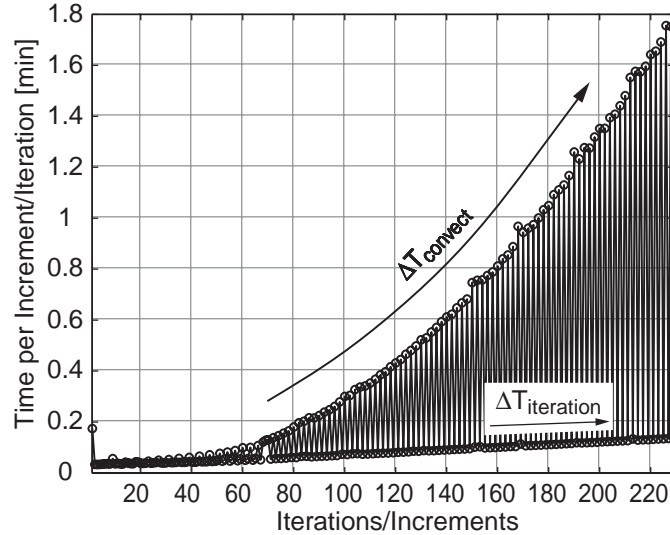


Figure 4.1: Simulation Time Versus Iterations/Increments

by  $\Delta T_{\text{convect}}$ , exhibits nearly exponential characteristics. On the contrary, the remainder of the simulation process per iteration/increment,  $\Delta T_{\text{iteration}}$ , only builds up linearly.

As discussed before, see Section 2.2.5, the wake records the history of the flow by storing the vorticity released from the trailing edges at every time step. By doing that, the wake enables the correct build up of surface velocities and pressures. Due to the  $1/r$  proportionality of induced velocities (see Biot-Savart Law), it is expected that only a finite number of downstream wake panels is required to ensure the accuracy of the solution. Once the wake panels have traveled a certain distance  $r$  away from the trailing edge their influence on the upstream bodies becomes negligible.

A convergence study with the unconfigured F16 wing model revealed that a good balance between accuracy of results and computational cost is reached when wake contributions over the past 40 increments are accounted for. This way, the wake works like a first-in-first-out (FIFO) buffer. The vorticities enter the wake from the trailing edge and are then shifted increment by increment through the wake for 40 time steps after which they are dismissed from the wake, i.e., the entire model. As summarized in Table 4.1, enlarging the wake results in a dramatic increase in computational cost with very little gain in accuracy. The error of the total lift for a 40-increment wake buffer, for instance, is within 1% of a 100-increment wake buffer, which is representative of a fully converged solution. It is obvious that the increase in computational cost outweighs by far the gain in accuracy. The other cases displayed in Table 4.1 are for parameters at the leading-edge/wing-tip location, where the solution turned out to be the most sensitive to the wake development. Even here it can



It takes about 78 increments for wing and pylon pressures to reach within 0.1% of their final values. This is not true, however, for the store model. The aerodynamic store model is of a different nature and the wake of the store exhibits very different characteristics than the corresponding wing and pylon wakes. Surface velocities on the store body reach their converged values a lot sooner than is the case for the wing and the pylon, but they also exhibit dependencies on airspeed and angle of attack. The number of increments needed for store surface velocities to reach within 0.1% of their final values increases from 34 to 47 at corresponding air speeds from Ma 0.5 to 0.8. This data is based on a static analysis of a wing/pylon/store model at a  $6^\circ$  AOA featuring the stiff-type pylon.

### Restarting the Analysis

By default ABAQUS provides the user with flexible restart capabilities, such that a previous analysis can be picked up and continued from any arbitrary point in time. This, of course, is of great use to the analyst and enhances productivity of the code dramatically. The merged aeroelastic code presented here features limited restart capabilities in the sense that any analysis can be continued from its end but not from within. Having ABAQUS linked to the UVLM complicates the restart procedure significantly. It is imperative that the two processes be synchronized correctly at the beginning of the restart analysis to ensure correct continuation of an old analysis. Because data coming from external routines are not written to the ABAQUS restart file, the load vector prior to the time of the restart must be re-established to initialize ABAQUS correctly. This task is accomplished through the governing handshake algorithm that for restart purposes features additional flag bits and synchronize cycles.

Being able to restart an analysis after completion has proven to be a valuable asset for analytical procedures. It is especially helpful, since different dynamic simulations can be launched from the same steady-state equilibrium. Once the model has reached steady-state for particular flow conditions, the results can be saved and made available to a dynamic continuation as often as desired. In addition, any dynamic simulation can be continued, in case the originally computed time history has not been run for enough time steps to show certain characteristics.

# Chapter 5

## Results

### 5.1 Static Analysis and Verification

The vortex lattice method employed in this work has been applied successfully to a variety of aerodynamic configurations such as delta wings, Rusak et al. [66], Seginer et al. [69], high aspect ratio wings, Hall [31], bridges, Preidikman and Mook [60], axisymmetric bodies, Özcan et al. [57], Rusak et al. [66], Almosnino [1], Presz and Pitkin [61], and store separation, Kayakayoglu [43]. Excellent agreement between experimental data and analytically obtained data has been reported when available. The following section demonstrates the validity of the UVLM for the case under consideration here. Both wing and store aerodynamics have been analyzed and compared against published data from other researchers. The pylon aerodynamics were not explicitly validated because the underlying numerical model is essentially identical to the wing model. By validating the wing model, the pylon model is implicitly verified.

#### The Wing

The distribution of the steady net-pressure coefficient, as it converges over the leading and trailing edges of the clean wing (CW) after the impulsive start is displayed in Figure 5.1 where the dashed line depicts the initial solution at time zero. As time progresses and the wake forms alongside the trailing edge and wing tip, the leading-edge values become stronger and the trailing edge values approach zero; over each chord section a typical airfoil pressure distribution evolves. The spatial distribution of the steady net-pressure displays a steady build up over the span until it drops sharply in the vicinity of the wing tip. Because the pressure data are obtained at panel control points, these discrete data do not provide values at the actual wing-tip chord section, where  $\Delta C_P$  equals zero. By the same token, the converged trailing-edge values are not exactly zero, but they are very close. The data were

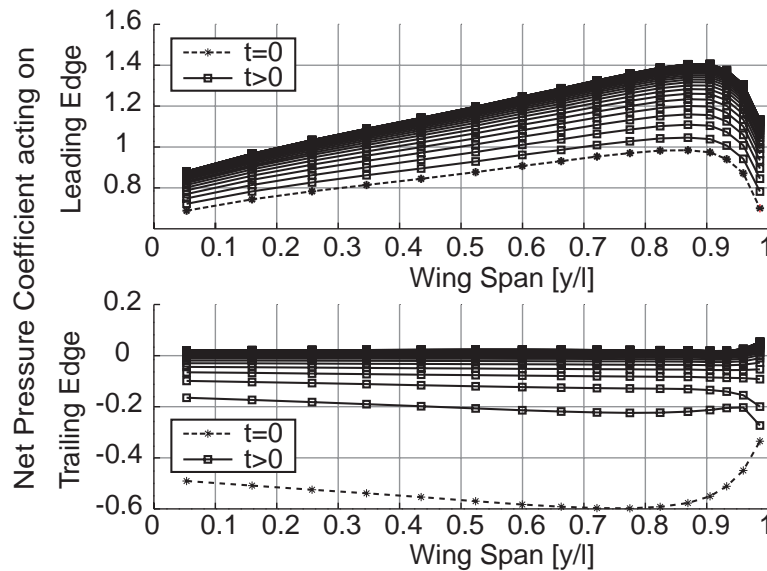


Figure 5.1: Wing Pressure Coefficient Distribution

extracted from a CW model travelling at 0.4 Ma at a 4° angle of attack (AOA).

The desire of the airflow to overcome the pressure discontinuity across the wing body results in a “flow” roll-up along the wing tip. This phenomenon, known as the wing-tip vortex, is common among lifting surfaces. Figure 5.2 qualitatively verifies the wing-tip vortex predictions of the proposed model. The photograph, Van Dyke [80], shows the trailing-edge

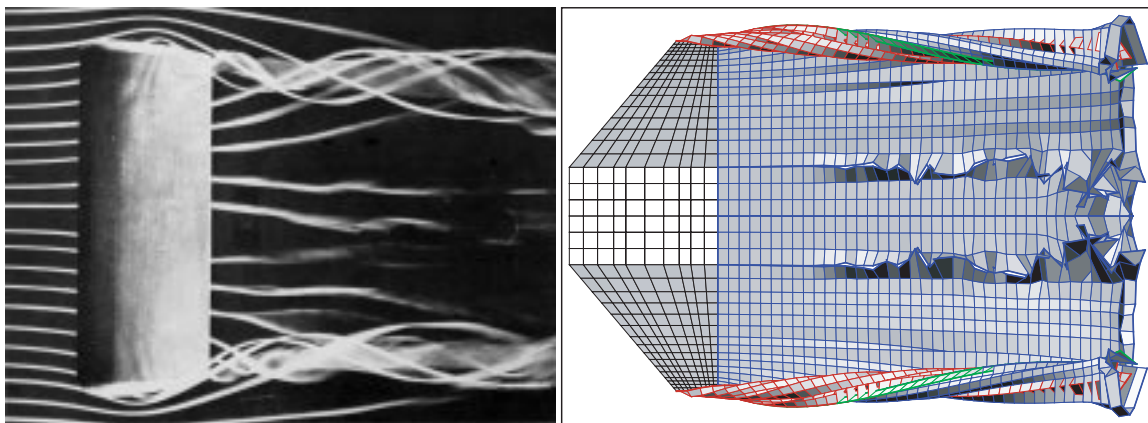


Figure 5.2: Verification of Wing Tip Vortex

vortices of a rectangular wing at 24° AOA and  $Re = 100,000$ , and the numerical result is the simulation of the clean wing at 0.4 Ma and 12° AOA. The simulation predicts qualitatively

the coherent vortex roll-up shown in the wind-tunnel experiment, validating the underlying aerodynamic model. It is worth pointing out that the numerical model is subject to cross wake interferences between the inboard section of the wing wake and the wake released from the fuselage. The picture of the experiment does not depict such behavior because the experiment features a full span wing model with one continuous trailing wake sheet.

## The Store

Figure 5.3 shows the lengthwise pressure distribution over the surface of the store body

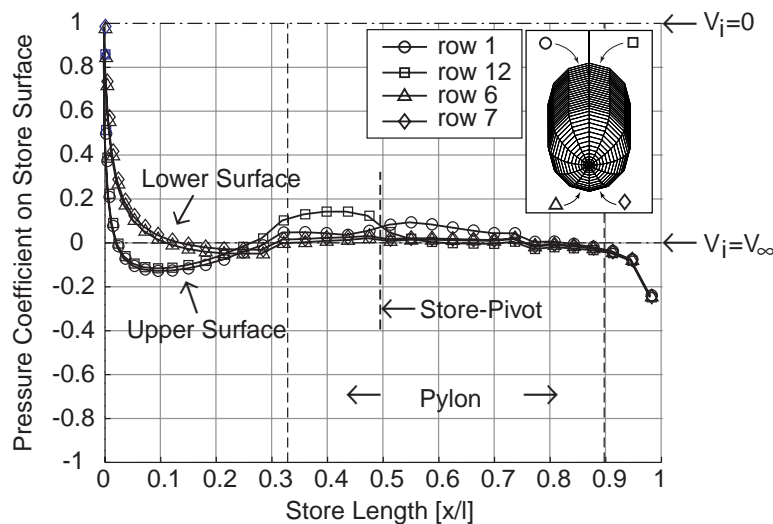


Figure 5.3: Store Pressure Coefficient Distribution

obtained from a simulation at  $0.4\text{Ma}$  and  $4^\circ$  AOA. The circular circumference of the store body is divided into a total of twelve lengthwise rows, of which rows one, twelve, six, and seven are depicted in the figure. Upper surface rows one and twelve as well as lower-surface rows six and seven are adjacent to each other, respectively. Rows twelve and seven are positioned inboard and rows one and six outboard of the pylon, see Figure 5.3. The separation of pressure values between the upper and lower surface along the store forebody indicates the existence of the small lift force previously identified in Figure 3.2. It is worth noting that pressures on the upper store surface alongside the pylon reflect the effects of the lateral barrier in the form of the pylon. Small velocity discontinuities between the two pylon-adjacent store rows are created because of the pylon induced lateral flow disruption. This influence is small and does not affect the other store rows. The pressures along these rows along the main part of the store body are that of the freestream. As the flow reaches the trailing edge of the store, it accelerates slightly as a result of the aft release into the free flow field. The above pressure curves are in excellent agreement with publications of experimental

and analytical research: see Özcan et al. [57], Presz and Pitkin [61]. As the flow speeds up over the trailing edge of the store, a reduction in the cross section of the emitting wake tube is a physical consequence. The wake tube envelopes the dead flow region that forms behind the store body and as the tube continuously decreases its diameter it eventually engages into an inward roll-up. The roll-up is a consequence of the conservation of vorticity and has been predicted by other researchers, e.g., Almosnino [1]. Unfortunately, this type of roll-up is inherently unstable since downstream wake panels are convected back inside the upstream wake tube. A physical flow, on the other hand, typically transition into a turbulent wake behind the dead flow region as shown in the photograph of Figure 5.4. Here a comparison between the wake coming from a flat-based body of revolution as depicted

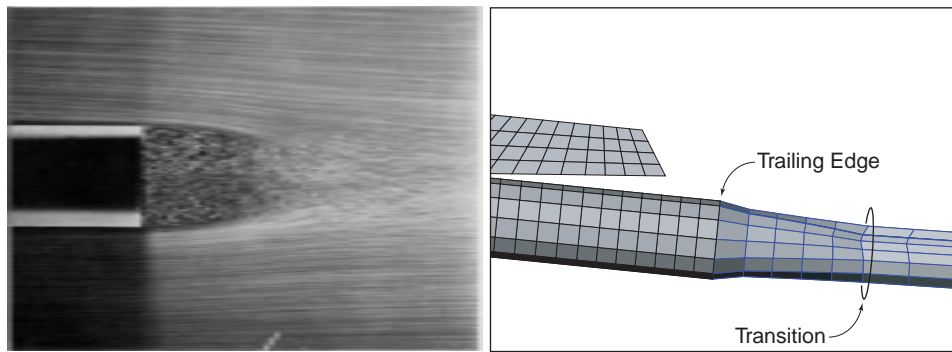


Figure 5.4: Verification of Store Trailing Edge Wake

by an ONERA photograph, Van Dyke [80], and the numerically predicted store wake at  $4^\circ$  AOA is shown. The numerical wake is set up to transition from the near wake into the far wake when the predicted inward roll-up would normally occur. To accomplish this, the far wake is convected without the influence of store body and store wake induced velocities. This numerical safeguard against wake instability proves to agree very well with physical observations. Furthermore, the far wake influence on store surface quantities is very small.

## 5.2 Clean Wing vs. Configured Wing

It is a commonly known fact among aeroelasticians that the presence of a pylon under the wing reduces the lift capabilities of the wing by disrupting the lateral flow on the lower wing surface. The code presented here predicts such losses very well, as can be seen in Figure 5.5. The figure displays an example for a  $4^\circ$  and  $8^\circ$  angle-of-attack wing/pylon/store configuration (WPS) cruising under steady-state conditions at  $0.4\text{Ma}$ . It demonstrates clearly how the outboard section of the wing suffers from a reduced, velocity differential between the lower and upper wing surface. As the lower-surface lateral flow is forced to accelerate past the pylon obstacle, it reaches a higher momentum which it retains throughout the remainder

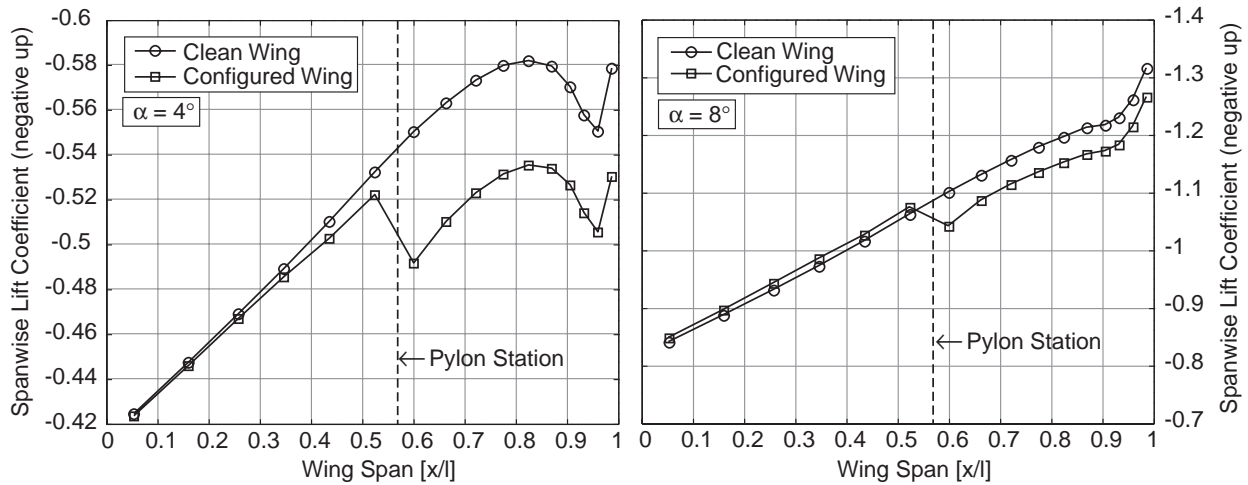


Figure 5.5: Spanwise Static  $C_L$  Distribution, Clean Wing and Configured Wing

of the outboard span. As a result, the velocity jump across the outboard wing region is reduced and the spanwise lift coefficient drops by a constant amount. By the same token, the underwing flow inboard of the pylon experiences a deceleration due to the lateral pylon barrier. The effect of the reduction in flow speed begins to take effect at higher AOA when the lift production inboard of the pylon increases over that of the clean wing. Under such circumstances, the store aerodynamics play a secondary role as far as their influence on the lifting surface is concerned. The above predictions agree well with experimental as well as analytical data, Triplett [76], Roos [64], published in the literature.

Figure 5.5 subsequently depicts the results of an aerodynamic phenomenon that occurs in the vicinity of the wing tip. The evolution of the wing-tip vortex has the effect of increasing the velocity difference across the wing tip. Consequently, the lift effectiveness in the outboard region of the of the wing improves, which is reflected by the sudden jump of  $C_L$  along the wing tip. Generally, the size and strength of the wing-tip vortex and its effect on the lifting-surface depends on the lift and aspect ratio of the wing. A high aspect ratio wing is less susceptible to wing-tip-vortex effects because the total lift is distributed over a larger span. For the low aspect ratio wing modeled here, increasing the lift on the wing and thereby making the trailing vortex stronger, progressively improves the lift along the outboard wing region as one can observe. To visualize this effect, the spanwise lift coefficient can be expressed in percent increase over its wing root value as a function of angle of attack. As shown in Figure 5.6, the influence of the trailing vortex, in fact, reaches all the way to the pylon station and eliminates the pylon induced lift-drop almost entirely. This result constitutes the unique quality of the model employed here. Production design tools such as NASTRAN that employ a standard doublet lattice method or horseshoe vortex lattice method are incapable of modeling these concepts because the underlying aerodynamics fail to account for the history of the flow,

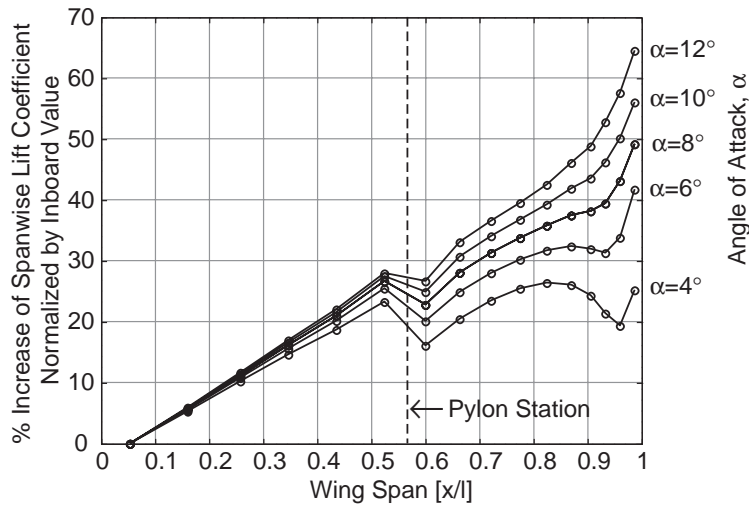


Figure 5.6: Effects of Wing Tip Vortex on Spanwise  $C_L$

captured in the wake.

Figure 5.7 collapses above observations into one plot. It depicts the total loss of lift versus

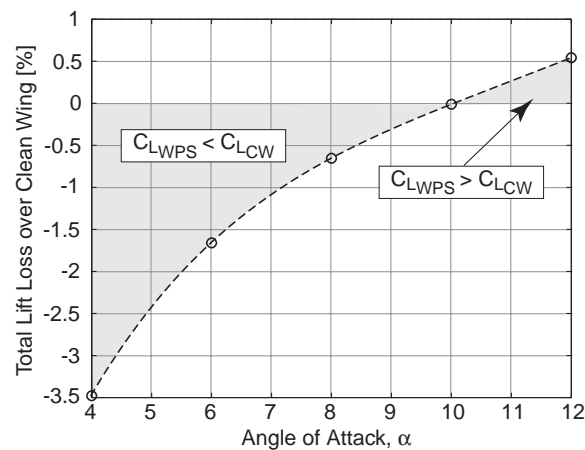


Figure 5.7: Lift Reduction due to Wing Configuration in Terms of  $C_L$

angle of attack due to the presence of the external pylon and store. It provides a more general picture of the overall effect of the external pylon/store attachment. It demonstrates how the lift advantage of the CW model over the WPS model is gradually eliminated as the AOA increases. In fact, the configured wing is projected to produce even more lift than the clean wing at high AOA.

### 5.3 Wake Analysis

The wake that forms as part of the solution in time is the historian of the flow. Once vorticity is released from a bound surface into the flow, it retains its strength forever — a consequence of the inviscid flow assumption. As a result of the wake propagation, the Kutta condition along trailing edges of bodies is enforced. The influence of the wake on the bound surfaces is consequently pronounced in regions of close proximity between bodies and wakes. The model under investigation features three independent bodies, each of which sheds a wake sheet, or tube in the case of the store, from its respective trailing edge. As the wakes are convected downstream they experience cross wake interference resulting in distortion of the clean wake sheets. The following section provides an analysis of this phenomenon in order to classify the effects such wake interference has on the upstream bodies. The following figures show the wake development of the semispan wing/pylon/store (WPS) configuration 0.4 s after the model has been perturbed from steady state at a velocity of Ma 0.8.

Figure 5.8 shows a side view of the wake development of the WPS model facing upstream under above conditions. At this instant in time the wing is subjected to a rapid down pitch motion producing a wave like shape of the wing wake. In the vicinity of the pylon, the wing

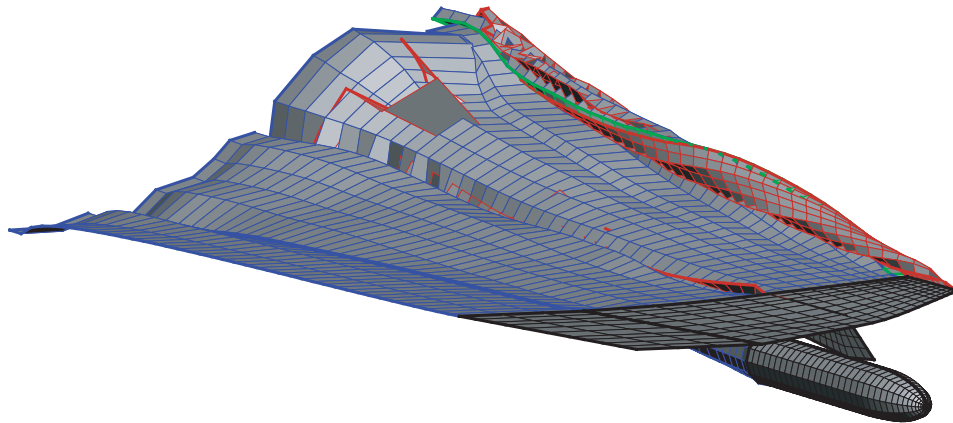


Figure 5.8: Wake Plot for Dynamic Analysis

wake is pulled downward as it interacts with the pylon wake forming a deep indentation in the wing wake aft of the pylon. Outboard of the pylon, the wing, store, and pylon wake interference is even more pronounced. The vortex roll-up along the wing tip pulls both pylon and store wakes alongside with it and amplifies the interference effects between the

three wake “bodies.” Figure 5.9 depicts a side view of the previous plot from a downstream position and reveals how the outboard section of the wing wake curls around the store wake. The pylon wake is confined inside the cone like shape of the wing wake and also curls

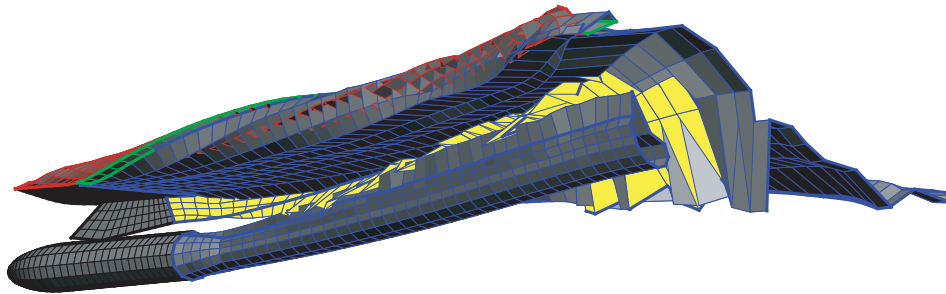


Figure 5.9: Wake Plot for Dynamic Analysis

around the store wake. The interaction between the different wakes is clearly noticeable, and a comparison with the WPS model that omits store and pylon aerodynamics (partial aerodynamic treatment) reveals that the shape of the wing wake is, in fact, very different from the full WPS model (full aerodynamic treatment). To that extent, Figure 5.10 contrasts both model versions with respect to their wake appearances viewed from head on. Both plots capture the same instant in time under the exact same conditions as mentioned above. The picture on the left shows the version of the full WPS model and the picture on the right shows the WPS model analyzed with wing aerodynamics only. The difference in the way the streamlines “flow” off the trailing edge of the wing is clearly noticeable. In light of such obvious differences it seems reasonable to expect changes in the pressure distributions across the wing between the two versions of the model. However, such propositions could not be confirmed. A close examination of time history of the lift development on the wing, as the wing oscillates, is given in Figure 5.11. The upper plot displays a total of four lift curves. Here the total lift is divided into inboard and outboard portions, where the pylon station is the dividing boarder line. The lower pair of curves depicts the lift on the outboard section of the wing and the upper pair depicts the lift on the inboard section. Each pair of curves contrasts the full WPS model and the partial WPS model. (The dashed vertical lines depict the instant in time at which above wake plots were taken.) As discussed in Section 5.1 the full WPS model experiences a spanwise lift increase inboard of the pylon

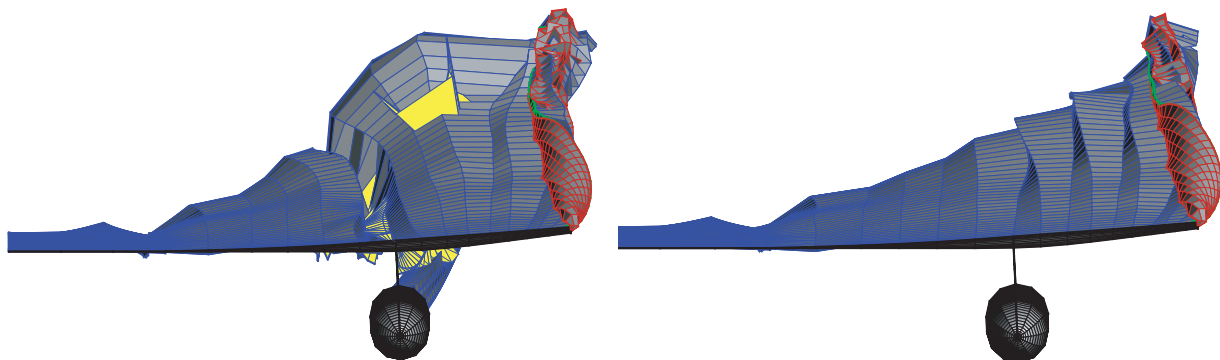


Figure 5.10: Wake Plot Comparison for Dynamic Analysis

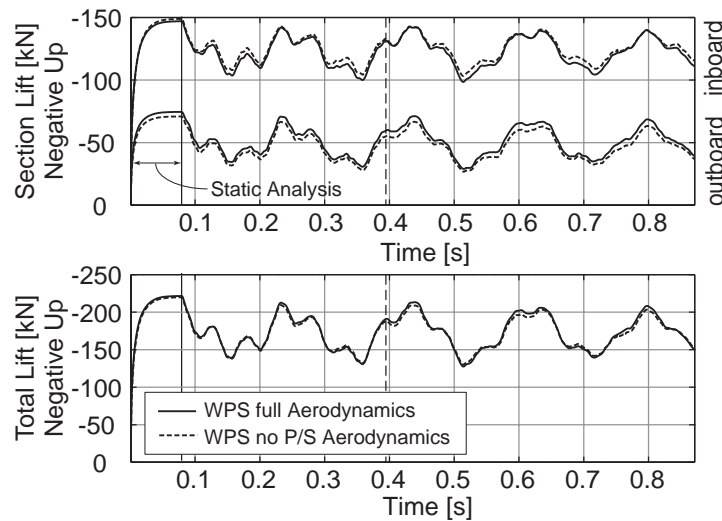


Figure 5.11: Time History of Dynamic Lift on Wing

and spanwise lift reduction outboard of the pylon in comparison to the lift distribution over an aerodynamically clean wing. These lift characteristics are retained throughout the history of the dynamic motion revealing no measurable effect induced by the downstream wake distortion. In fact, the total lift on the wing, as depicted by the lower plot of Figure 5.11, is essentially the same between the two versions of the WPS model. There are some very small periodic discrepancies that are attributed to the slightly larger up pitch motion of the wing when store aerodynamics are omitted. Such motion increases the local angle of attack momentarily and results in a periodically increased lift production over that of the fully treated WPS model. However, the wing wake distortion itself, caused by the pylon and store wakes, has no immediate bearing on the lift characteristics of the wing. The predicted aerodynamic interference effects take place too far downstream to impact on the upstream

bodies for the scenario investigated here.

Although aerodynamic interference effects between wakes could not be established as a contributing factor in wing/store systems, they are likely to have an effect on bodies that lie in their downstream path, see Elzebda et al. [22, 20, 21], such as horizontal or vertical tails. Such scenarios occur typically when the airplane undergoes turn maneuvers during which the wing-tip vortex can be projected onto the tail structure. This can induce violent buffeting of vertical tails as has been reported for twin tail aircraft such as the F15 or F18. Finally, the unique way in which the wake is predicted as part of the solution process offers great insight into nature of the flow and is a most valuable asset in understanding the physics of the fluid-structure interaction examined here.

## 5.4 Dynamic Analysis

The purpose of the analysis undertaken here is to investigate the dynamic characteristics of the wing/pylon/store (WPS) model. To accomplish this, the time histories of the response were recorded after the model was perturbed from steady state at different airspeeds. The goal was to establish the flutter capabilities of the model and to subsequently verify the concept of the decoupler pylon. As part of this investigation, the store aerodynamics and their contribution to the flutter behavior are classified. It is not the intention to reproduce actual F16 characteristics, e.g., flutter reported in the literature, because the structural model employed here is not properly tuned to the real structure due to lack of actual F16 data.

### Flutter Investigation

This section is provided to demonstrate functionality of the aeroelastic WPS model by verifying dynamic principles of fluid-structure interaction with respect to airspeed. The model was subjected to airspeeds varying from Ma 0.4 to 0.8, where the upper velocity bound is a consequence of the flow assumptions postulated in Section 2.2. At the beginning of each analysis, the first 80 increments are a static analysis to establish steady-state conditions. After that, the analysis is continued dynamically starting with a one-increment impulse excitation to induce both bending and torsion. The time history of the response is recorded for about 1.2 seconds and postprocessed using MATLAB. Such a short analysis time is sufficient to classify tendencies of the dynamic response because three to four periods of the fundamental modes are contained within this time frame. Figure 5.12 shows a plot of the time response at the wing tip of the WPS model featuring the production pylon. The time history is depicted at two different air speeds: Ma 0.6 and 0.8. It is evident that the model subjected to the higher airspeed experiences a form of self-excitation, as indicated by the repeated amplitude increase after 0.8 s. The displacement curve itself provides good evidence that the oscillatory

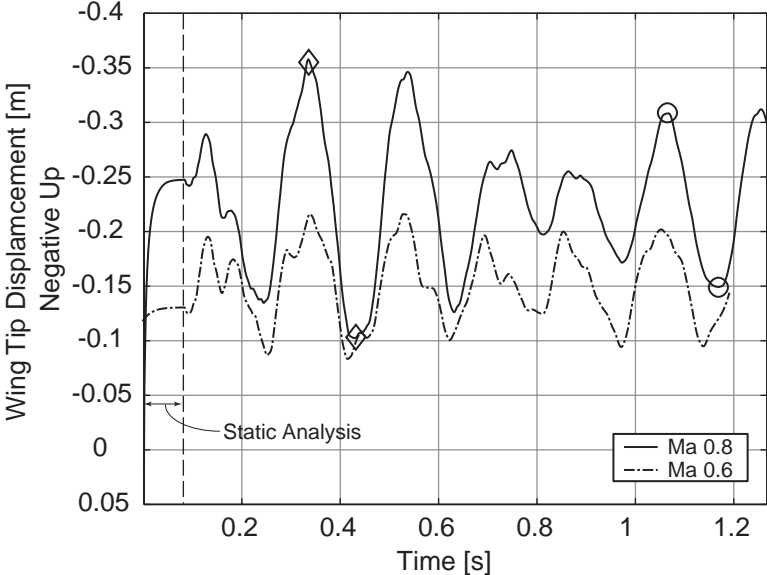


Figure 5.12: Wing Tip Time Response for Production Pylon Model

motion is dominated by a single frequency. When computed, this frequency is in the range of 5 to 5.15 Hz — the time history is still too short to allow more exact determination of the dominant frequency. In comparison, the time signal obtained at the lower velocity clearly shows participation of at least two distinct frequencies, and the analysis of the entire wing motion reveals that these two frequencies belong to the first bending mode and the first torsion or store-pitch mode. Figure 5.13 shows the maximum peak deflections of the WPS

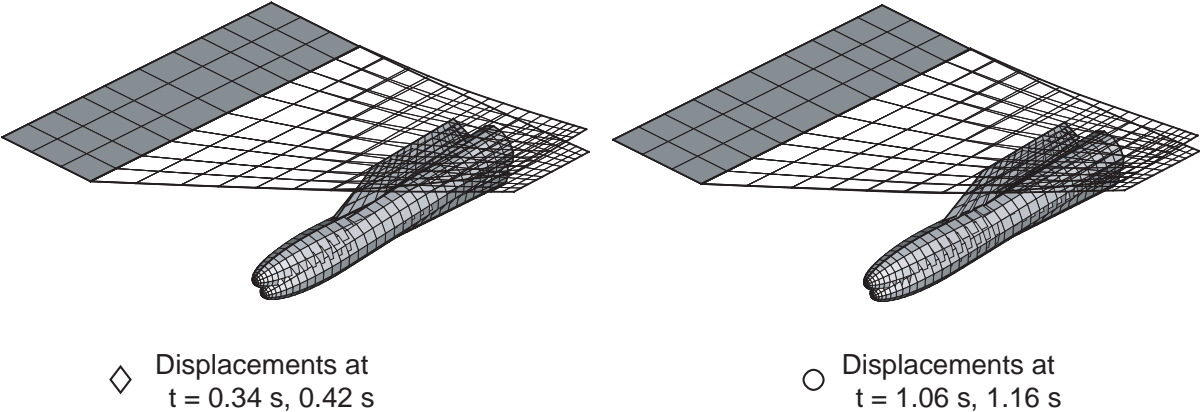


Figure 5.13: WPS Peak Deflection under Near Flutter Conditions

model at Ma 0.8 for two different half cycles in time. On the left, the half cycle depicts the motion around time  $t = 0.4$  s, see diamonds in Figure 5.12, and on the right, it depicts the motion around time  $t = 1.1$  s, see circles in Figure 5.12. As was the case for the model at the lower airspeed, both first bending and torsional modes participate in the motion; only this time the corresponding frequencies are very close, if not identical. Finally, results from analyzing the eigenfrequency-versus-airspeed relationship a range of freestream velocities are summarized in Figure 5.14. It substantiates the observation that the model undergoes

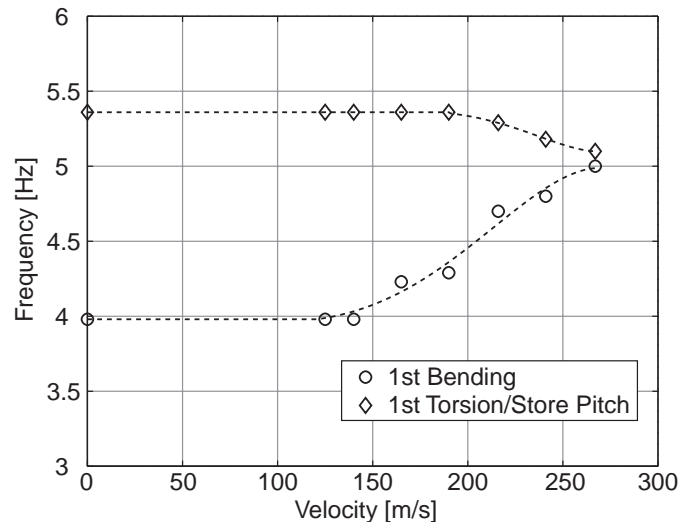


Figure 5.14: Frequency Versus Velocity for Production Pylon Model

bending-torsion motion of coalescent frequencies. All observations point toward the fact that the model has reached the vicinity of its critical airspeed at Ma 0.8. The shortness of the recorded time histories, however, allows no conclusive classification of the true state of fluid-structure interaction. The detected motion could resemble limit cycle oscillations, or the motion could simply decay over time like signals at lower airspeeds. Longer time signals are necessary to determine the characteristics with reliable accuracy. In light of the fact that the model is a parametric representation of the F16 wing configuration, elaborate investigations are not feasible until a better structural model becomes available. The above investigation demonstrates the functionality of the proposed model and gives confidence in the developed methodology of solving the aeroelastic equation of motion.

## Decoupler Pylon

To assess the principle of the decoupler pylon, the close-to-critical speed scenario from the previous section is considered but with the soft pylon instead of the “rigid” production pylon. Figure 5.15 displays the time history of the wing-tip deflection in the upper part

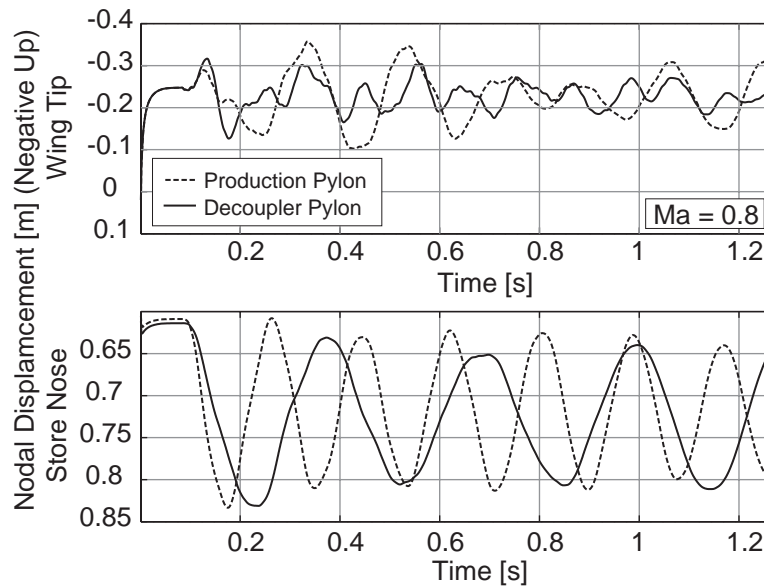


Figure 5.15: Decoupler Pylon Model Versus Production Pylon Model

and the store tip deflection in the lower part. It is clearly noticeable how the production pylon WPS model exhibits much larger wing-tip deflections than the model featuring the decoupler pylon. Whereas the wing-tip deflection increases again during the later part of the time history for the stiff pylon configuration, it continuously decays when the decoupler pylon is implemented. Attached to the decoupler pylon, the store pitches at its zero-speed natural frequency of 3.1 Hz, whereas the store mounted to the production pylon undergoes pitch oscillations of 5.1 Hz, coalescent with the nearly merged bending-torsion frequency of the whole structure.

As expected, the soft pylon decouples the wing-torsion mode from the store-pitch mode, resulting in a more stable WPS configuration. The simulation reveals that the decoupled store-pitch mode is not susceptible to increasing flow velocities. Consequently, when the pitch stiffness is designed to place the store-pitch frequency below the fundamental wing-bending frequency, a coupling between store-pitch and wing bending as airspeed increases is not expected. The decoupler pylon also prevents coalescence of wing-bending and -torsion frequencies at the identified “critical” speed because it enlarges the spread between the two modal frequencies by approximately 39% (see Section 3.1).

### Store Aerodynamics

To investigate the contributions of store and pylon aerodynamics for flutter analysis, the WPS model was compared to a model that omits store and pylon aerodynamics altogether. Figure 5.16 presents the wing-tip deflection of the two versions of the WPS model for the

near-flutter case analyzed above. As indicated in Section 5.3, a larger pitch-up motion of the

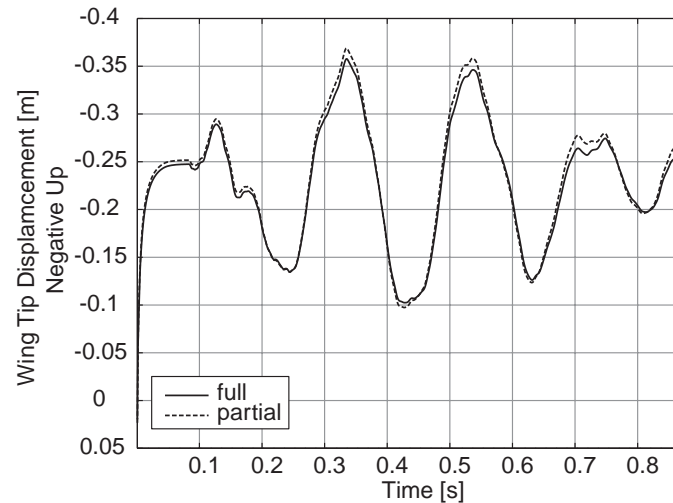


Figure 5.16: Full Aerodynamic Treatment Versus Partial Treatment

wing can be observed when store and pylon aerodynamics are omitted. This effect, of course, is small and of no consequence to the characteristics of the solution. As postulated by many researchers in the field, aerodynamic effects on the store and pylon can be neglected for typical wing/store flutter investigations. There are several cases that require aerodynamic treatment of the store and pylon, and the proposed model provides the ideal environment to investigate such behavior:

- Unsymmetric flow separation along the store surface can induce limit cycle oscillations of the store body. High angle-of-attack situations usually lead to an adverse pressure gradient on the upper store surface in the vicinity of which the flow is provoked to separate. As a result, the aerodynamic loading on the surface can become unsymmetric thereby inducing pitch motion which can lead to limit cycles. Although the currently employed aerodynamic code does not include flow separation on surfaces, it is possible to extend the model to include such phenomena.
- Consideration of store aerodynamics is essential for store separation analysis. Store release is a dangerous procedure for the airplanes involved. It is not uncommon that a released store is lifted up by aerodynamic forces into the flight path of the airplane.
- Maneuver loads on store and pylon increase the aerodynamic loading of both pylon and store which subsequently strengthens the respective wakes. Such conditions could result in more pronounced wake interference effects than for the cases investigated here.

### Computational Cost

Computational cost is quite intense which is part of the reason why the obtained time signals are relatively short. The entire code is installed on an Origin 2000 computer featuring eight R100000 processors and two Gigabytes of RAM. By default ABAQUS engages in parallel processing between four processors whereas the UVLM has not been designed to take advantage of the parallel processing environment. The UVLM is written in FORTRAN 90 and is compiled using the “-O3” option to optimize memory allocation of the compiled code and subsequently decrease computation time by approximately 50% over the version using nonoptimized compilation. A simulation of 400 time increments, during each of which the code iterates three times, requires between 18 and 19 hours of runtime for the full WPS model. Omitting store and pylon aerodynamics speeds up simulation time by about 80%, e.g., to simulate 1.27 seconds at Ma0.8 takes 9.5 hours for the partial WPS model and 54 hours for the full WPS model. Naturally, the full WPS model is not the recommended choice for wing flutter investigations of wing/store systems.

# Chapter 6

## Summary, Contributions, and Future Work

### Summary

The goal of this work was to develop an advanced aeroelastic tool that can subsequently be used to analyze flutter and limit cycle oscillations (LCO) of aircraft carrying underwing stores. Many of the mechanisms that lead to oscillatory behavior of wing/pylon/store configurations are still not fully understood, and there exists a need to provide engineers with comprehensive tools to further advance this research. The driving force behind this research is the desire to make aircraft safer, more energy efficient, and to reduce maintenance intensity. Limited amplitude flutter and limit cycle oscillations cause fatigue in the structure resulting in premature material failure and increase the overall energy consumption of the system. It has been a long pursued hypothesis that nonlinear aerodynamic forces are the predominant cause of such behavior. To that extent, there exists a great variety of numerical CFD codes and aeroelastic software packages that capture aerodynamic effects in their full complexity. In recent years, however, researchers have begun to consider nonlinear structural mechanisms, such as Coulomb friction, as a possible trigger for the observed LCO behavior.

The modular code, developed here, features ABAQUS/Standard, a commercial, fully nonlinear, structural dynamics finite element code to provide the utmost flexibility for structural coherence with the “real world model.” To enable aeroelastic treatment of fluid-structure models, the unsteady vortex-lattice method (UVLM) was linked to the FEM code by means of a handshake mechanism that coordinates the data exchange between the host process, ABAQUS, and the slave process, UVLM. The unsteady vortex-lattice method was chosen because it allows treatment of unsteady and nonlinear flow phenomena at relatively low computational cost (in comparison to full scale CFD codes) and for its unique capabilities in providing the wake as part of the solution. Because the UVLM captures the history of the flow in the wake, investigation of wing-tip-vortex influences and cross-wake aerodynamic

interference can be undertaken. Consequently, store as well as pylon aerodynamics are modeled comprehensively to provide for the respective wakes that are shed from the trailing edges of these bodies.

Predictions of the complete aeroelastic code were qualitatively validated against published analytical/numerical and experimental data. Because accurate data about the wing of the F16 has not been released to the public, quantitative validation of aerodynamic as well as structural data, e.g., mode shapes or lift properties of the wing, was not possible. An elementary flutter investigation was undertaken to demonstrate the functionality of the two-entity aeroelastic model. This investigation included reproducing the concept of the decoupler pylon, i.e., demonstrating that flutter speed can be increased by flexibly mounting external stores to the wing. The proposed parametric wing/pylon/store model of the F16 promises to be an effective tool in analyzing aeroelastic fluid-structure problems. In fact, the model can be used at airspeeds that technically exceed the subsonic range. The airspeed and the model stiffness are kinematically related, and when one applies airspeeds beyond the inviscid flow boundaries one essentially obtains a model of lower stiffness subjected to subsonic flow. If one wishes to achieve better coherence with the real F16 structure it is necessary to obtain more complete information about the wing of the F16.

## Contributions

A new numerical method has been developed that provides fully nonlinear, aeroelastic, analysis of fluid-structure-interaction mechanisms of wing/store configurations. The model shows excellent qualitative agreement with currently accepted results from published literature. The code models key-phenomena of fluid-structure interaction in wing/store analysis:

- Lateral flow disruption due to the underwing pylon is predicted correctly and resulted in inboard lift increase and outboard lift reduction.
- An increase of lift in the region of the wing tip is correctly predicted as a result of the wing tip vortex which locally increases the pressure difference between upper and lower wing surface.
- The model reproduces the concept of the decoupler pylon successfully. At a speed of  $Ma 0.8$ , the model with a standard production pylon experiences near bending-torsion flutter conditions of 5.1 Hz, whereas the model with the decoupler pylon remains clearly stable.

Additionally, the code features the wake as part of the solution which provides the foundation to analyzing wake interference mechanisms and leading-edge separation scenarios and allows great insight into the nature of the flow. For the dynamic cases under investigation, aerodynamic interference between pylon/store and wing wake has been found to have negligible effects on the lift and drag of the wing.

The proposed aeroelastic ABAQUS/UVLM software demonstrated its unique capabilities in capturing the essence of wing/store interaction and is projected to help better understand the mechanisms involved in nonlinear LCO and flutter behavior.

Contributions of this work can be summarized as follows:

- Extended linear two-dimensional wing/store flutter model to fully nonlinear three-dimensional model.
- Created a new methodology for examining fluid-structure interaction for wing/store systems.
  - Developed and coded a handshake mechanism to govern data exchange between ABAQUS and the UVLM.
  - Extended UVLM-based aerodynamic part of stand-alone aeroelastic wing code, Preidikman [59], to include pylon and store aerodynamics.
  - Incorporated full restart capabilities for continuation of preceding analysis.
  - Provided the means to analyze wake interference effects of wing/store systems which can be used to establish lift and drag disturbances caused by the wake on bodies that are in the downstream path of the wake.
- Verified model predictions against published standards and validated functionality.
  - Phenomenon of wing tip vortex increases lift in the region of the wing tip.
  - Lateral flow disruption due to wing-mounted pylon resulting in inboard lift increase and outboard lift reduction.
  - Flutter speed can be increased by means of the decoupler pylon, i.e., by reducing pylon pitch stiffness from “rigid” to soft.
  - Store and pylon aerodynamics are negligible in analyzing flutter characteristics of the wing/store system, in accordance to the widely accepted assumption that store aerodynamics can be ignored.

## Future Work

The research presented here provides the means to analyze aeroelastic phenomena with a unique balance between structural dynamics and aerodynamics. In continuation of this research it is compelling to generate a full-span model including fuselage inertia and mass properties together with free-free boundary conditions. This would allow one to examine asymmetric mode shapes and rigid body modes as they exist in reality. A full-span model would also provide the necessary completeness to model roll and yaw motion of the entire airplane making it possible to examine effects of the underwing pylon and store even more

comprehensively. Furthermore a tail section could be added to the fuselage to examine effects of the wake when tail bodies enter the downstream path of the wake.

The ease at which the structure can be adapted in ABAQUS to exhibit desired characteristics makes it possible to engage flutter and LCO investigations employing various nonlinear elements. Because the aerodynamic model does not need to be changed for flutter investigations, examining different store configurations also becomes a fairly straightforward task.

Additionally, the model provides suitable analytic capabilities for adaptive wing structures, such as the morphing wing projects many airplane manufacturers are working on to date. Such applications are inherently nonlinear and are a perfect fit for this analytic tool.

# Bibliography

- [1] D. Almosnino. High angle of attack calculations of the subsonic vortex flow on slender bodies. *AIAA Journal*, 23(8):1150–1156, 1985.
- [2] D. Almosnino and J. Rom. Calculation of symmetric vortex separation affecting subsonic bodies at high incidence. *AIAA Journal*, 21:398–406, 1983.
- [3] B. Bennekers, R. Roos, and R. J. Zwaan. Calculation of aerodynamic loads on oscillating wing/store combinations in subsonic flow. In *AGARD Specialists Meeting on Wing-with-Stores Flutter*, number 4, pages CP–162, München, 1974.
- [4] John. J. Bertin and Michael L. Smith. *Aerodynamics for Engineers*. Prentice Hall, third edition, 1998.
- [5] Raymond L. Bisplinghoff, Holt Ashley, and Robert L. Halfman. *Aeroelasticity*. Dover Publictaions, Inc., reprinted edition, 1996.
- [6] Fung. Y. C. *An Introduction to the Theory of Aeroelasticity*. Dover Publications, Inc., reprinted edition, 1993.
- [7] J. Cattarius, S. Preidikman, D. T. Mook, and D. J. Inman. Vortex-lattice-method to analyze aerodynamic interference of wing/pylon/store configurations of an f16 wing. In *CEAS/AIAA/ICASE/NASA Langley International Forum on Aeroelasticity and Structural Dynamics*, volume PT2 of *CP-1999-209136*, pages 443–455, JUNE 1999.
- [8] F. W. Cazier, Jr. and M. W. Kehoe. Ground vibration test of F-16 airplane with initial decoupler pylon. Technical Memorandum NASA-TM-86259, NASA, 1984.
- [9] F. W. Cazier, Jr. and M. W. Kehoe. Flight test of a decoupler pylon for wing/store flutter suppression. In *AIAA Flight Testing Conference*, volume 1 of 3, 1986.
- [10] F. W. Cazier, Jr. and M. W. Kehoe. Flight test of passive wing/store flutter suppression. Technical Memorandum NASA-TM 877661, NASA, 1986.
- [11] F. W. Cazier, Jr. and M. W. Kehoe. Ground vibration test on an F-16 airplane with modified decoupler pylons. Technical Memorandum NASA-TM-87634, NASA, 1986.

- [12] A. Cenko. PanAir applications to complex configurations. *AIAA 21st Aerospace Sciences Meeting*, 1983.
- [13] A. Cenko and E. Tinoco. PanAir applications to mutual interference effects due to close proximity. *AIAA 22nd Aerospace Science Meeting*, 1984.
- [14] A. Cenko, E. N. Tinoco, R. D. Dyer, and J. DeJongh. PanAir application to weapons carriage and separation. *Journal of Aircraft*, 18(2):128–134, 1980.
- [15] P. C. Chen and D. D. Liu. Unsteady supersonic computations of arbitrary wing-body configurations including external stores. In *AIAA, Structural Dynamics and Materials Conference*, number 29, pages 794–812, 1988.
- [16] I. G. Currie. *Fundamental Mechanics of Fluids*. McGraw-Hill, Inc., second edition, 1993.
- [17] G. Deferrari, L. Chesta, O. Sensburg, and A. Lotze. Effects on nonlinearities on wing/store flutter. *AGARD Math. Modeling of Linear and Non-Linear Aircraft Struct.*, pages 15–32, 1980.
- [18] R. N. Desmarais and W. H. Reed, III. Wing/store flutter with nonlinear pylon stiffness. *Journal of Aircraft*, 18(11):984–987, 1980.
- [19] Earl H. Dowell and Marat Ilgamov. *Studies in Nonlinear Aeroelasticity*. Springer-Verlag, 1988.
- [20] J. M. Elzebda, D. T. Mook, and A. H. Nayfeh. Unsteady aerodynamic interference for lifting surfaces. In *AIAA 12th Atmospheric Flight Mechanics Conference*, number AIAA-85-1801-CP, 1985.
- [21] J. M. Elzebda, D. T. Mook, and A. H. Nayfeh. Steady and unsteady aerodynamic interference in closely coupled canard/wing configurations. In *Forum on Unsteady Flow Separation ASME Fluid Engineering Spring Conference*, 1987.
- [22] J. M. Elzebda, D. T. Mook, and A. H. Nayfeh. Numerical simulation of steady and unsteady, vorticity-dominated aerodynamic interference. *Journal of Aircraft*, 31(5): 1031–1036, 1994.
- [23] L. Fornasier. HISSS — a higher-order subsonic/supersonic singularity method for calculating linearized potential flow. In *AIAA 17th Fluid Dynamics, Plasma Dynamics, and Laser Conference*, 1984.
- [24] Prasad V. N. Gade and George T. Flowers. Flutter suppression of an airfoil with unsteady forces using a piezoelectric active strut. In *AIAA/ASME Adaptive Structures Forum*, 1994.

- [25] Prasad V. N. Gade and Daniel J. Inman. Controller design for wing/store flutter suppression of an airfoil in incompressible flow. In *AIAA Structural Dynamics and Materials Conference*, number AIAA-96-1633, pages 221–229, 1996.
- [26] Prasad V. N. Gade and Daniel J. Inman.  $H_\infty$  controller design for wing/store flutter suppression. In *ASME 1996 International Mechanical Engineering Congress and Exposition*, volume 193 of *Active Control of Vibration and Noise*, pages 91–99, 1996.
- [27] Prasad V. N. Gade and Daniel J. Inman. Uncertainty models and associated trade-offs for wing/store flutter suppression. In *SPIE Far East and Pacific Rim Smart Materials, Structures and MEMS Conference*, page 90, 1996.
- [28] Prasad V. N. Gade and Daniel J. Inman. 2-d active wing/store flutter suppression using h-infinity theory. *AIAA Journal of Guidance, Control and Dynamics*, 20(5):949–955, 1997.
- [29] Prasad V. N. Gade and Daniel J. Inman. Active control of store induced flutter in incompressible flow. *Journal of Aircraft*, 35(3):454–461, 1998.
- [30] Prasad V. N. Gade and Daniel J. Inman. Robust adaptive control of store release event for wings with external stores. *AIAA Journal of Guidance, Control and Dynamics*, 22(3):408–414, 1999.
- [31] Benjamin D. Hall. Numerical simulations of the aeroelastic response of an actively controlled flexible wing. Master’s thesis, Virginia Polytechnic Institute and State University, 1999.
- [32] C. A. Harvey, G. Stein, and L. R. Felt. Adaptive control of wing/store flutter — a feasibility study. In *AIAA Struct., Struct. Dyn. and Mater. Conference*, pages 296–304, 1979.
- [33] J. Heeg. An analytical and experimental investigation of flutter suppression via piezoelectric actuation. Technical Report AIAA-92-2106-CP, AIAA, 1992.
- [34] *ABAQUS/Standard Users Manual*. Hibbitt, Karlsson & Sorensen, Inc., 1999.
- [35] R. M. Hicks, S. E. Cliff, R. G. Melton, R. G. Langhi, A. M. Goodsell, D. D. Robertson, and S. A. Moyer. Euler and potential computational results for selected aerodynamic configurations. In P. A. Henne, editor, *Applied Computational Aerodynamics*, volume 125 of *Progress in Astronautics and Aeronautics*, pages 263–388. American Institute of Aeronautics and Astronautics, Inc., 1990.
- [36] Ming T. Ho and Roger. R. Chen. Unified approach of active panel vibration and flutter controls using piezoelectric actuation and iterative root locus method. In *ASME Design Engineering Technical Conferences*, 1997.

- [37] Terry L. Holst. Numerical solution of the full potential equation using a chimera grid approach. *AIAA Journal*, 35(9):1543–1545, 1997.
- [38] H. Hönlinger. Design and testing of an active vibration and flutter damping system for external stores. In *DGLR Symp. CCV Technol.*, 1976.
- [39] E. H. Johnson, C. Hwang, D. S. Joshi, C. A. Harvey, L. T. Huttzell, and M. G Farmer. Adaptive flutter suppression, analysis and test. *AGARD Recent Transonic Flutter Invest. for Wings and External Stores 12p*, 1983.
- [40] T. L. Johnson, C. A. Harvey, and G. Stein. Self-tuning regulator design for adaptive control of aircraft wing/store flutter. *IEEE Transactions on Automatic Control*, AC-27(5):1014–1023, 1982.
- [41] Robert T. Jones. *Wing Theory*. Princeton Academic Press, first edition, 1990.
- [42] Krishnamurty Karamcheti. *Principles of Ideal-Fluid Aerodynamics*. Krieger Publishing Company, reprinted edition, 1980.
- [43] Ruhi Kayakayoglu. Unsteady subsonic aerodynamics for maneuvering wing/fuselage/pylon/store configuration and store separation including wake effects. Progress Report N97-71841, Wright Labs, 1993.
- [44] P. Konstadinopoulos, D. T. Mook, and A. H. Nayfeh. A numerical method for general unsteady aerodynamics. In *AIAA Atmospheric Flight Mechanics Conference*, 1981.
- [45] P. Konstadinopoulos, D. F. Thrasher, D. T. Mook, A. H. Nayfeh, and L. Watson. A vortex-lattice method for general, unsteady aerodynamics. *Journal of Aircraft*, 22(1):43–49, 1985.
- [46] Michael W. Lai, David Rubin, and Erhard Krempl. *Introduction to Continuum Mechanics*. Butterworth-Heinemann Ltd, third edition, 1993.
- [47] Michael D. Madson and Larry L. Ericksons. Toward the routine aerodynamic analysis of complex configurations. In P. A. Henne, editor, *Applied Computational Aerodynamics*, volume 125 of *Progress in Astronautics and Aeronautics*, pages 701–752. American Institute of Aeronautics and Astronautics, Inc., 1990.
- [48] J. A. Main and E. Garcia. Piezoelectric stack actuators and control system design: Strategies and pitfalls. *Journal of Guidance, Control, and Dynamics*, 1997.
- [49] M. P. Mignolet, D. D. Liu, and P. C. Chen. On the nonlinear structural damping mechanism of wing/store limit cycle oscillation. In *AIAA/ASME/ASCE/AHS/ASC Structures, Struc. Dyn., and Materials Conference and Exhibit*, volume 3, pages 2148–2161, 1999.

- [50] D. T. Mook and J. A. Luton. Numerical simulations of interactions among aerodynamics, structural dynamics, and control systems. Virginia Polytechnic Institute and State University, December 1996.
- [51] D. T. Mook and A. H. Nayfeh. Application of the vortex-lattice method to high-angle-of-attack subsonic aerodynamics. In *Aerospace Technology Conference & Exposition*, 1985.
- [52] D. T. Mook and A. H. Nayfeh. Numerical simulation of dynamic/aerodynamic interactions. *Computing Systems in Engineering*, 1(2-4):461–482, 1990.
- [53] D. T. Mook and A. O. Nuhait. Simulation of the interaction between aerodynamics and vehicle dynamics in general unsteady ground effect. In *Intersociety Advanced Marine Vehicles Conference*, 1989.
- [54] A. H. Nayfeh, D. T. Mook, and A. Yen. The aerodynamic of small harmonic oscillations around large angles of attack. In *AIAA, 12th Fluid and Plasma Dynamics Conference*, 1979.
- [55] T. E. Noll, L. J. Huttsel, and D. E. Cooley. Wing/store flutter suppression investigation. *Journal of Aircraft*, 18(11):969–975, 1981.
- [56] T. E. Noll, L. J. Huttsell, and D. E. Cooley. Investigation of international control laws for wing/store flutter suppression. In *AIAA 21st. Struct., Struct. Dyn. and Mater. Conf.*, number pt2, pages 585–594, 1980.
- [57] O. Özcan, M. F. Ünal, A. R. Aslan, Y. Bozkurt, and N. H. Aydin. Aerodynamic characteristics of external store configurations at low speeds. *Journal of Aircraft*, 32(1): 161–170, 1995.
- [58] R. P. Peloubet, Jr., R. L. Haller, and R. M. Bolding. On-line adaptive control of unstable aircraft wing flutter. In *IEEE, Conference on Decision and Control*, volume 2 of 29, pages 643–651, 1990.
- [59] Sergio Preidikman. *Numerical Simulations of Interactions Among Aerodynamics, Structural Dynamics, and Control Systems*. PhD thesis, Virginia Polytechnic Institute and State University, 1998.
- [60] Sergio. Preidikman and D. T. Mook. A new method for actively suppressing flutter of suspension bridges. *Wind engineering and industrial aerodynamics*, 69(71):955–974, 1997.
- [61] Walter M. Presz, Jr and Edward T. Pitkin. Flow separation over axisymmetric aftbody models. *AIAA Journal*, (AIAA 74-17), 1974.
- [62] Wilmer H. Reed, III, F. W. Cazier, Jr., and Jerome T. Foughner, Jr. Passive control of wing/store flutter. Technical Memorandum NASA TM-81865, NASA, 1980.

- [63] Wilmer H. Reed, III, Jerome T. Foughner, Jr., and Harry L. Runyan, Jr. Decoupler pylon: A simple, effective wing/store flutter suppressor. *Journal of Aircraft*, 17:206–211, 1980.
- [64] R. Roos. Unsteady airloads on a harmonically pitching wing with external store. In *AIAA/ASME 21st Struct., Structural Dyn. and Mater. Conference*, number pt1, pages 409–416, 1980.
- [65] R. Roos, B. Bennekers, and R. J. Zwaan. Calculation of unsteady subsonic flow about harmonically oscillating wing/body configurations. *Journal of Aircraft*, 14(5):447–454, 1977.
- [66] Z. Rusak, A. Seginer, and E. Wasserstrom. Convergence characteristics of a vortex-lattice method for nonlinear configuration aerodynamics. *Journal of Aircraft*, 22(9):743–749, 1985.
- [67] Z. Rusak, E. Wasserstrom, and A. Seginer. Numerical calculations of nonlinear aerodynamics of wing-body configurations. *AIAA Journal*, 21(7):929–936, 1983.
- [68] S. S. Samant, J. E. Bussoletti, F. T. Johnson, R. H. Burkhart, B. L. Everson, and R. G. Melvin. TranAir: A complex code for transonic analysis of arbitrary configurations. In *AIAA 25th Aerospace Sciences Meeting*, 1987.
- [69] A. Seginer, Z. Rusak, and E. Wasserstrom. Convergence characteristics of nonlinear vortex-lattice methods for configuration aerodynamics. Technical Report AIAA 83-1882, AIAA, 1982.
- [70] O. Sensburg, H. Hönlinger, and T. E. Moll. Active flutter suppression on an F-4F aircraft with external stores using already existing control surfaces. In *AIAA, 21st Struct., Struct. Dyn. and Mater. Conference*, 1980.
- [71] O. Sensburg, H. Hönlinger, T. E. Noll, and L. J. Huttzell. Active flutter suppression on an f-4f aircraft. *Journal of Aircraft*, 19(5):354–359, 1982.
- [72] H. C. “Skip” Smith. *The Illustrated Guide to Aerodynamics*. McGraw Hill, first edition, 1996.
- [73] Deman Tang and Earl H. Dowell. Unsteady aerodynamic forces and aeroelastic response for external store of an aircraft. *Journal of Aircraft*, 35(5):678–687, 1998.
- [74] Edward N. Tinoco. CFD applications to complex configurations: A survey. In P. A. Henne, editor, *Applied Computational Aerodynamics*, volume 125 of *Progress in Astronautics and Aeronautics*, pages 559–616. American Institute of Aeronautics and Astronautics, Inc., 1990.

- [75] H. Triebstein, G. Schewe, H. Zingel, and S. Vogel. Measurement of unsteady airloads on an oscillating engine and a wing/pylon combination. *Journal of Aircraft*, 31(1):97–102, 1994.
- [76] W. E. Triplett. Wind tunnel correlation study of aerodynamic modeling for F/A-18 wing/store tip-missile flutter. *Journal of Aircraft*, 21:329–334, 1984.
- [77] W. E. Triplett, H.-P. F. Kappus, and R. J. Landy. Active flutter control — an adaptable application to wing/store flutter. *Journal of Aircraft*, 10(11):669–678, 1973.
- [78] C. D. Turner. A study of the effects of store aerodynamics on wing/store flutter. Thesis, Virginia Tech, 1980.
- [79] Gerrit J. van den Broek. The use of a panel method in the prediction of external store separation. *Journal of Aircraft*, 21(5):309–315, 1984.
- [80] Milton Van Dyke. *An Album of Fluid Motion*. The Parabolic Press, 1982.
- [81] J. W. G. Vannunen, R. Roos, and J. J. Meijer. Investigation of the unsteady airloads on wing/store configurations in subsonic flow. In *AGARD Fluid Dyn. Panel. Sump. on Unsteady Aerodyn.*, pages 22–28, 1977.
- [82] Y. R. Yang. KBM method of analyzing limit cycle flutter of a wing with an external store and comparison with a wind-tunnel test. *Journal of Sound and Vibration*, 187(2): 271–280, 1995.
- [83] Zhi-Chun Yang and Ling-Cheng Zhao. Wing/store flutter analysis of an airfoil in incompressible flow. *Journal of Aircraft*, 26:583–587, 1989.
- [84] Zhi-Chun Yang, Ling-Cheng Zhao, and Jie-Sheng Jiang. Effects of pylon yaw and lateral stiffness on the flutter of a delta wing with external store. In *International Modal Analysis Conference, Proceedings*, volume 2 of 11, pages 1466–1470, 1993.
- [85] H. Zimmerman and S. Vogel. Influence of main design parameters on flutter behaviour for aircraft configurations with heavy concentrated masses. In *AGARD, Aeroelastic Considerations in the Preliminary design of aircraft*, number 11p, 1983.

# Appendix A

## Complementary Figures

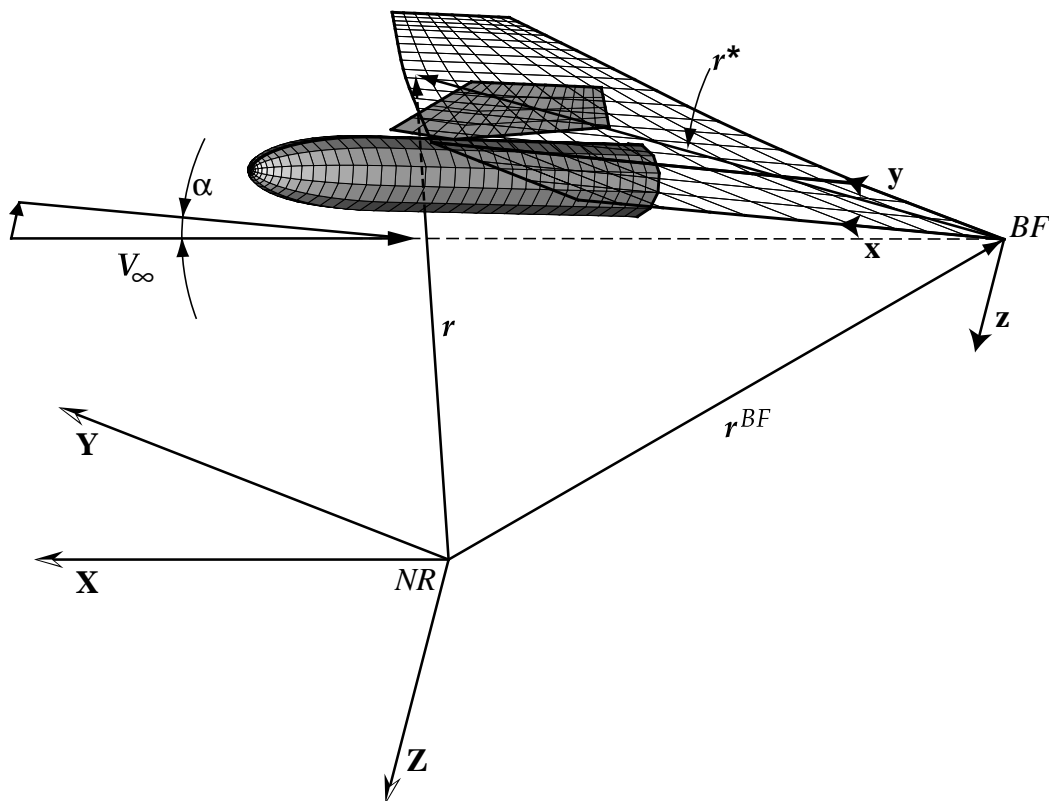


Figure A.1: Coordinate Systems



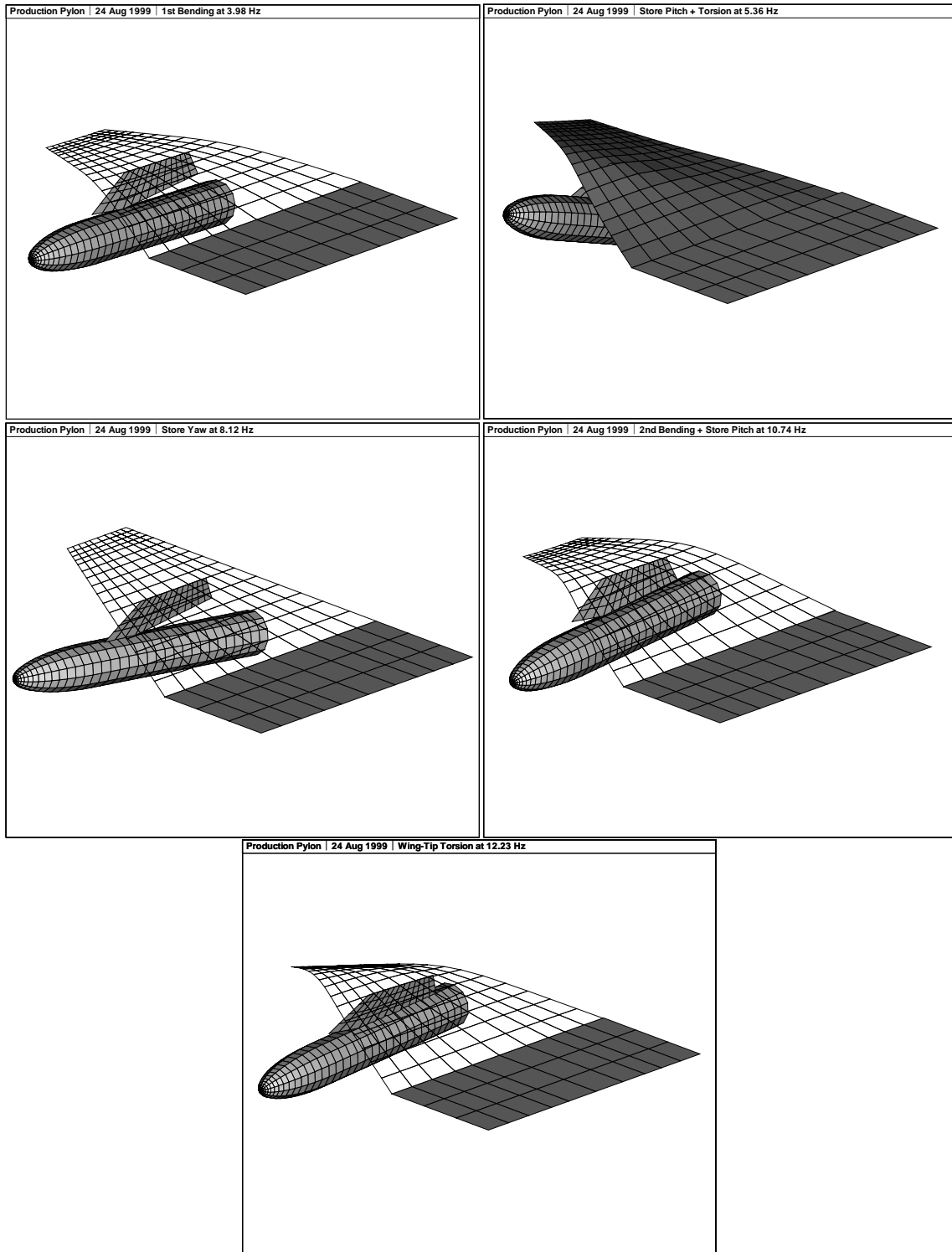


Figure A.3: Clamped-Symmetric Mode Shapes of PP Configuration

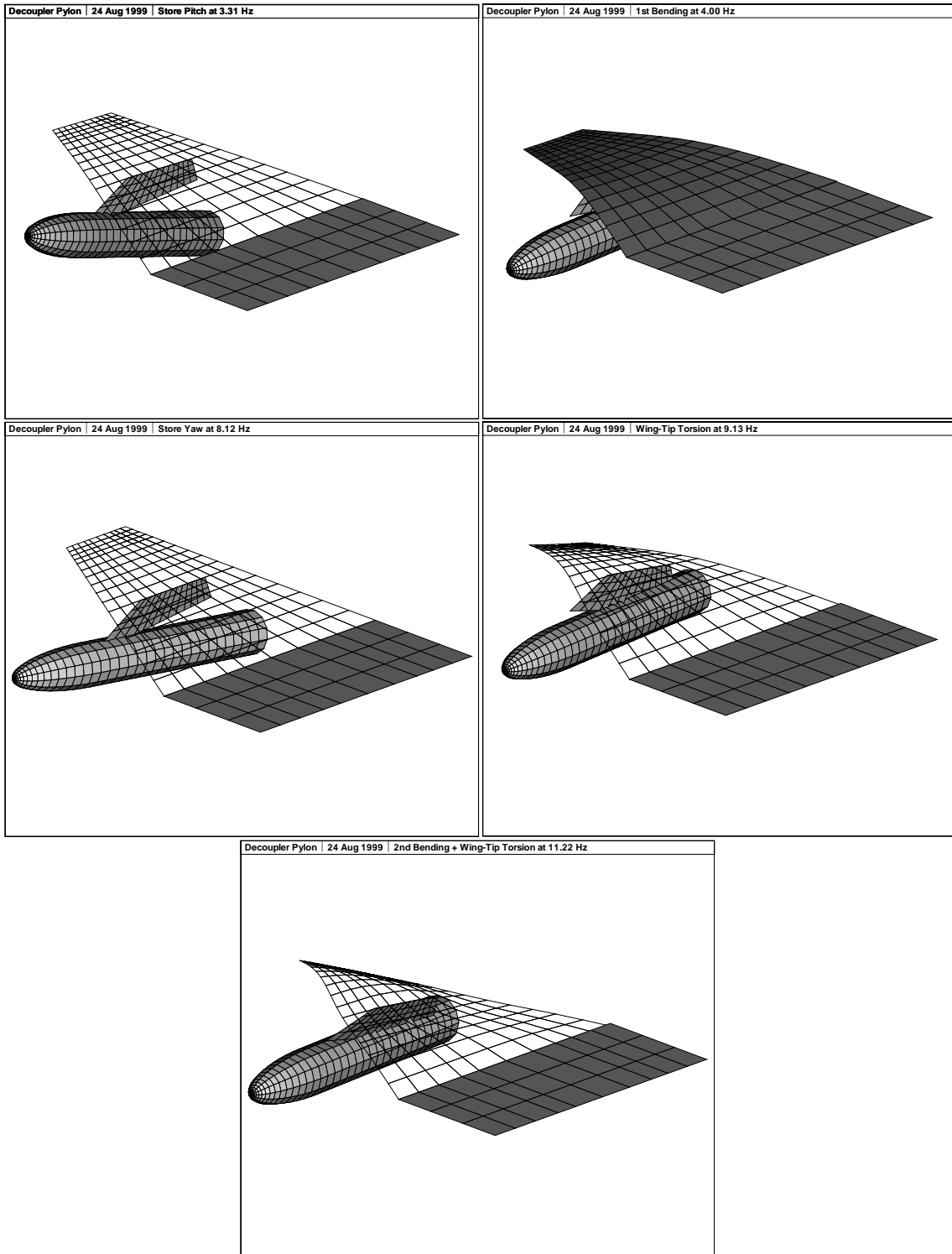


Figure A.4: Clamped-Symmetric Mode Shapes of DP Configuration

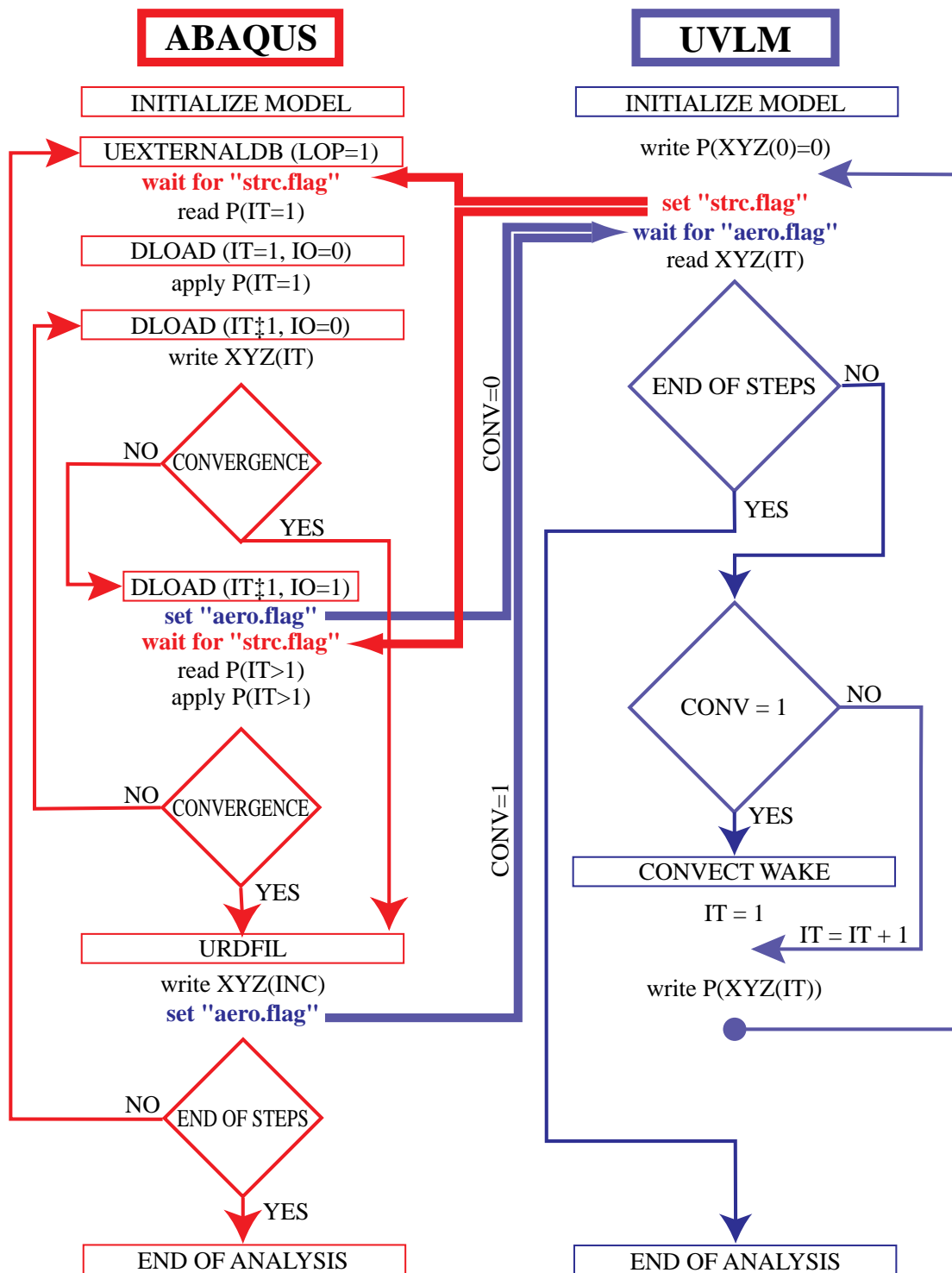


Figure A.5: Handshake Flow Chart

# Vita

Jens was born in Kusel, Germany, on June 1, 1968, the first child of Lothar and Waltraud Cattarius. In August of 1993 he graduated with the degree of *Diplom-Ingenieur* in Electrical Engineering from the *Technische Universität Darmstadt* in Germany. During the final three years of his studies he worked part time as an assistant system administrator for *Schott Glaswerke* in Mainz, Germany. In December of 1993 he came to Virginia Tech to work under Dr. Daniel J. Inman as a research assistant in the field of damage detection. Jens' work was awarded a full-time research scholarship through the Center of Intelligent Materials, Systems, and Structures in January of 1994 which enabled him to continue his research appointment for one more year. Following this appointment, Jens went back to Germany for four months and returned to Blacksburg in August of 1995 to enroll as a graduate student at Virginia Tech to pursue a doctorate degree in Engineering Mechanics under Dr. Daniel J. Inman. On June 25 he married the former Melissa Susanne Goode, and upon graduation Jens and Melissa will move to Germany where Jens will begin a job appointment with DaimlerChrysler in Stuttgart, Germany.